Large-eddy simulations of turbulent wake flows behind helical- and straight-bladed vertical axis wind turbines rotating at low tip speed ratios

Masoumeh Gharaati[,1] Shuolin Xiao[,1,*] Luis A. Martínez-Tossas[,2]
Daniel B. Araya,[3] and Di Yang[1,†]

[1]*Department of Mechanical Engineering, University of Houston, Houston, Texas 77204, USA*
[2]*National Renewable Energy Laboratory, Golden, Colorado 80401, USA*
[3]*Johns Hopkins University Applied Physics Laboratory, Laurel, Maryland 20723, USA*

Turbulent wake flows behind helical- and straight-bladed vertical axis wind turbines (VAWTs) rotating at low tip speed ratios (TSRs) are studied numerically. The turbulent flows are simulated using the large-eddy simulation (LES) model, and the rotating turbine blades are modeled using the actuator line method. The helical VAWT has identical key parameters as the straight VAWT except for the 135° helical twist of the blades over the 0.3 m vertical span. A set of LES runs are performed for two TSRs, 0.6 and 0.4, and the results are reported and analyzed. At these low TSRs, the wake behind the straight-bladed VAWT exhibits two-dimensional dominant flow motions (in the horizontal plane perpendicular to the straight blades) in the near-wake region that cause considerable spanwise expansion of the wake as it extends downstream. In contrast, the helical-bladed VAWT generates highly three-dimensional (3D) wake flow structures and upward/downward mean flow motions within the wake that cause the wake to expand mainly in the vertical direction. Turbulence statistical analyses also show that the 3D wake flow features induced by the helical blades accelerate the wake transition to turbulence and enhance the small-scale turbulent dissipation (as shown by the subgrid-scale turbulent dissipation in the LES), which leads to a more rapid decay of the wake turbulence intensity than that in the straight-bladed VAWT case at the same TSR. Compared with the straight-bladed VAWT, the helical-bladed VAWT also exhibits much smaller temporal variations for the torque and power coefficients during the rotation cycle, which can be beneficial for wind power generation.

I. INTRODUCTION

As a clean and renewable energy resource, in recent years wind energy has achieved continuous growth in market share globally [1,2]. Wind energy is harvested mainly by using wind turbines, which can be categorized into two main types based on the orientation of the turbine rotor axis: the horizontal axis wind turbines (HAWTs) and the vertical axis wind turbines (VAWTs) [3,4]. Large size HAWTs (i.e., exceeding 100 m in hub height and rotor diameter) have gained success and popularity in commercial wind farms because of their generally high rated power and energy-conversion efficiencies [4,5]. On the other hand, VAWTs have also attracted increasing interest in recent years due to the easier maintenance and operation (e.g., ground-mounted electrical components, no complex yaw-control required, insensitive to wind direction, etc.) [6], potentially

---

*Present address: Department of Mechanical Engineering, Johns Hopkins University, Baltimore, Maryland 21218, USA.

†Contact author: diyang@uh.edu

faster wake recovery [7], and relatively small footprint for application. These features make VAWT a feasible choice for wind energy harvest in urban environments where land areas are usually limited.

In recent years, noticeable research efforts have been devoted to studying the aerodynamics and wake flow characteristics of VAWTs [8–30]. Various important aspects of the design that affect the VAWT performance and wake flow characteristics have been studied, e.g., the number of blades [14,21,23], the rotor diameter-to-height aspect ratio [16,28], the blade dynamic stall [9,12,19,24,25], the blade pitch control [30], the VAWT tip speed ratio (TSR) [10,11,13,20,21,23], etc. Note that most of these studies have considered VAWTs that operate at moderate TSRs (i.e., about 1.0–4.0). For potential installations and operations in urban environments, VAWTs with even lower TSRs (i.e., lower than 1.0) may be desired due to the low noise level [24,31–34] and reduced harm in case of an accidental blade strike [35]. Parker and Leftwich [36] and Araya *et al.* [23] have shown that the VAWT wake flow characteristics exhibit considerable variations as the TSR changes, suggesting that the knowledge obtained by studying VAWTs of higher TSRs may not be directly applicable to characterize those with lower TSRs.

Moreover, various types of VAWT designs differ mainly by the blade geometries. Examples include the Savonius turbines, the Darrieus turbines with curved blades, the straight-bladed Darrieus turbines, and the helical-bladed Darrieus turbines [21,33]. Among them, the straight-bladed Darrieus-type VAWTs have been studied and utilized more than other types [8,15,17,18,22–24,26,27,29], likely due to the simpleness of its design for easy manufacturing. A number of laboratory [8,15,17,22] and field [7,18,37] experiments as well as numerical simulations [24,38–42] of straight-bladed VAWTs have helped advance our knowledge on both the fundamental characteristics of the turbine wakes and the dynamic interactions of the VAWTs with atmospheric boundary layer turbulence if deployed in the field. The helical-bladed VAWTs, which can be regarded as the twisted version of the straight-bladed VAWTs, have not been studied extensively but have gained increasing attention [29,43–47]. For example, Cheng *et al.* [45] performed two-dimensional (2D) large-eddy simulation (LES) and three-dimensional (3D) unsteady Reynolds-averaged Navier–Stokes (URANS) modeling of a four-blade helical VAWT at TSRs ranging from 0.9 to 2.3 and focused on quantifying the power coefficient. By comparing the results of 2D LES and 3D URANS, they found the power coefficient obtained from 3D URANS to be about 33.3% lower than that obtained from 2D LES, and thus they concluded that effort should be devoted to eliminating 3D aerodynamic effects in order to improve the performance of helical-bladed VAWTs. However, a 2D LES is inherently unable to capture any 3D effect that should be expected from the 3D geometry of the helical-bladed VAWT. 2D turbulence is also known to exhibit some fundamental differences from 3D turbulence [48–51], making the choice of using 2D LES to study flow past 3D helical-bladed VAWT uncertain. Another URANS-based study was performed by Divakaran *et al.* [46], who modeled three-blade helical VAWTs with various helix angles rotating at TSRs ranging from 2.3 to 3.9.

Recently, Wei *et al.* [29] performed field experiments using the 3D particle-tracking velocimetry to measure the wind velocity and vorticity fields around a full-scale three-blade helical VAWT (with a vertical rotor height of 3.2 m and a rotor diameter of 1.8 m) rotating at TSRs 1.19 and 1.40, as well as another full-scale five-blade straight VAWT (with a vertical rotor height of 3.7 m and a rotor diameter of 2.2 m) rotating at TSRs 0.96 and 1.20. They obtained the time-averaged velocities and vorticities on various orthogonal 2D planes across the turbine rotor center and at several downstream cross sections, the combination of which provided the 3D time-averaged flow structures in the near-wake region of the two VAWTs. By matching the key parameters of the three-blade helical VAWT in Wei *et al.* [29], Gharaati *et al.* [47] used LES with the actuator line turbine model to simulate the long-range wake development (up to about 25 rotor diameters downstream) of the helical-bladed VAWT in a boundary layer turbulence with consistent wind speed and TSR (1.19) as reported in Wei *et al.* [29], and compared the wake characteristics to that of a straight-bladed VAWT with identical parameters except for the blade geometry. Gharaati *et al.* [47] also considered an additional helical-bladed VAWT with the blade twist direction reversed, based on which they confirmed that

the effects induced by the helical blades also got reversed. Both Wei *et al.* [29] and Gharaati *et al.* [47] observed a net mean vertical flow motion along the center line of the wake behind the helical-bladed VAWT, which affects the wake development and the turbulence statistics when compared with the wake behind the straight-bladed VAWT. Note that the full-scale helical-bladed VAWT considered in Wei *et al.* [29] and Gharaati *et al.* [47] was designed for commercial wind power production. Despite the new findings obtained from the above experimental and numerical studies, our knowledge is still limited regarding the performance and wake flow characteristics of smaller size helical VAWTs with lower operational TSRs that are suitable for potential applications in urban environments.

In this study, we perform numerical simulations to investigate the effects of helical and straight blades on the VAWT wake flow characteristics at TSRs below 1.0. We use the same LES model as the one used by Gharaati *et al.* [47]. LES is able to resolve a wide range of turbulent flow motions directly and has been widely used as a research tool for studying wind turbine and wind farm flows [52–56]. In our study, two laboratory-scale VAWTs with identical key parameters but different blade geometries (one with straight blades and the other with helical blades) are considered. Each VAWT has a rotor diameter of 0.3 m and a rotor vertical height of 0.3 m, and consists of five blades with a cross-sectional profile of the NACA0018 airfoil and a chord length of 0.043 m. Both the straight- and helical-bladed VAWTs rotate counterclockwise under wind forcing. For the helical-bladed VAWT, each blade has a total twist angle of $135°$ counterclockwise from top to bottom. Within the LES model, the VAWT blades are modeled using the actuator line method (ALM), which has been successfully used in prior LES studies of HAWTs and VAWTs [24,38–42,55–61]. To isolate the effect of blade geometry from other potential factors that may affect the VAWT wake characteristics, in the present LES study a turbulent inflow condition with uniform mean velocity is used. Similar uniform mean inflow conditions have been used in prior studies of VAWTs in both laboratory experiments [8,15,17,20,22,23,27] and numerical simulations [24,38,40]. Particularly, in this study the inflow condition consists of a uniform mean velocity and a homogeneous isotropic turbulence (HIT) velocity fluctuation field. The HIT component is constructed using the data extracted from the Johns Hopkins Turbulence Database (JHTDB) [62] and is implemented into the LES using the method proposed in Martínez-Tossas *et al.* [63]. The mean wind speed in the simulation is set to be 13 m/s, for which the corresponding TSR of the turbine rotation is set to be 0.6 based on the wind-tunnel tests of the two VAWTs. In addition, a lower TSR of 0.4 is also considered for comparison purposes. The simulation data obtained from the LES runs are analyzed, and comparison between the wake flow statistics of the helical- and straight-bladed VAWTs are made to help elucidate the potential benefits of utilizing the helical-bladed VAWT design for urban environment applications.

The remainder of this paper is organized as follows. The LES model for simulating VAWT wake flow is briefly described in Sec. II, with more details given in the Appendixes. Section III summarizes the setup of the simulation cases. In Sec. IV the VAWT wake flows are characterized by direct observation and statistical analysis, and the effects of the VAWT blade geometry are elucidated by comparing the wakes behind straight- and helical-bladed VAWTs. Finally, conclusions are given in Sec. V.

II. LARGE-EDDY SIMULATION MODEL FOR WIND-VAWT INTERACTION

In the present study, the large-eddy simulation model LESGO developed by the Johns Hopkins University Turbulence Research Group is adopted as the main turbulence flow solver [64]. LESGO has been successfully used to model wind turbine wake flows in several LES-based studies [52,53,58,59,63,65,66]. LESGO is formulated based on 3D Cartesian coordinates $x_i(i = 1, 2, 3) = (x, y, z)$, where x, y, and z are for the streamwise, spanwise, and vertical directions, respectively. The corresponding velocity components in x, y, and z directions are denoted as $u_i(i = 1, 2, 3) = (u, v, w)$, respectively.

The turbulent flow around the VAWT is simulated by solving the filtered Navier-Stokes equations in rotational form [67–69],

$$\frac{\partial \widetilde{u}_i}{\partial x_i} = 0, \tag{1}$$

$$\frac{\partial \widetilde{u}_i}{\partial t} + \widetilde{u}_j \left(\frac{\partial \widetilde{u}_i}{\partial x_j} - \frac{\partial \widetilde{u}_j}{\partial x_i} \right) = -\frac{\partial \widetilde{p}^*}{\partial x_i} + \nu \frac{\partial^2 \widetilde{u}_i}{\partial x_j \partial x_j} - \frac{\partial \tau_{ij}^d}{\partial x_j} - \frac{f_{\epsilon,i}}{\rho}. \tag{2}$$

Here the tilde denotes filtering at the LES grid scale Δ; $\widetilde{u}_i$ is the resolved flow velocity; ρ is the density of air; ν is the kinematic viscosity of air; $\tau_{ij}^{sgs} = (\widetilde{u_i u_j} - \widetilde{u}_i \widetilde{u}_j)$ is the unresolved subgrid-scale (SGS) stress tensor, and $\tau_{ij}^d = \tau_{ij}^{sgs} - \delta_{ij} \tau_{kk}^{sgs}/3$ is the deviatoric (trace-free) part of τ_{ij}^{sgs}, where δ_{ij} is the Kronecker delta; $\widetilde{p}^* = \widetilde{p}/\rho + \widetilde{u}_k \widetilde{u}_k/2 + \tau_{kk}^{sgs}/3$ is the pseudopressure, where $\widetilde{p}$ is the resolved dynamic pressure; and $f_{\epsilon,i}$ is the distributed body force for modeling the turbine-induced aerodynamic forces on the air flow. In the current LES model, $f_{\epsilon,i}$ is modeled using ALM [57]. More details of the implementation of ALM in the current LES model are given in Appendix A.

In the present study, τ_{ij}^d is parameterized using the Lilly-Smagorinsky eddy-viscosity-type model [70,71], $\tau_{ij}^d = -2\nu_{sgs}\widetilde{S}_{ij} = -2(c_s\Delta)|\widetilde{S}|\widetilde{S}_{ij}$, where $\widetilde{S}_{ij} = 0.5(\partial \widetilde{u}_j/\partial x_i + \partial \widetilde{u}_i/\partial x_j)$ is the resolved strain-rate tensor, $|\widetilde{S}| = \sqrt{2\widetilde{S}_{ij}\widetilde{S}_{ij}}$ is the strain-rate magnitude, and $\nu_{sgs} = (c_s\Delta)|\widetilde{S}|$ is the modeled SGS eddy viscosity. The Smagorinsky model coefficient c_s is determined dynamically during the simulation using the Lagrangian-averaged scale-dependent dynamic (LASD) model [72]. The LASD model has been successfully applied in several prior LES studies of wind turbine wake flows [47,52–54,65,66,73–75].

In LESGO model, a Fourier-series-based pseudospectral method based on collocated grids is used for the spatial discretizations in the x and y directions, and a second-order central-difference method based on staggered grids is used for the spatial discretization in the z direction. The 3/2 rule is used to eliminate the aliasing error associated with the pseudospectral discretization of the nonlinear convective terms [76]. The periodic boundary condition is used in the spanwise direction, and the stress-free condition is applied at the top and bottom boundaries in the vertical direction. In the streamwise direction, the inflow–outflow conditions are used in order to model the turbine wake flow. More details of the inflow–outflow conditions implemented in the current pseudospectral solver are given in Appendix B.

The simulation is advanced in time using a fractional-step method. First, the velocity field is advanced in time by integrating Eq. (2) using the second-order Adams-Bashforth scheme to obtain a predicted velocity field. Then a pressure Poisson equation is constructed based on the divergence-free constraint Eq. (1) for the new time step and is solved to obtain the pseudopressure field. Lastly, the predicted velocity field is projected to the divergence-free space using the gradient of the pseudopressure to obtain the velocity field for the new time step. The above fractional steps are repeated at every time step in LES to advance the flow field in time. More details of the numerical schemes used in the LESGO model can be found in Albertson [77] and Albertson and Parlange [69].

III. SETUP OF SIMULATION CASES

In this study, one helical-bladed VAWT and one straight-bladed VAWT are considered, as shown in the photos in Fig. 1. Both VAWTs have identical key parameters as shown in Table I. In particular, the turbine rotor diameter is $D = 2R = 0.3$ m; the turbine rotor height (i.e., the vertical distance between the top and bottom edges of each turbine blade) is $H = 0.3$ m; each VAWT is composed of $N_b = 5$ blades with a cross-sectional profile of a NACA0018 airfoil (with a chord length of $c = 4.3$ cm and a thickness of $t_b = 0.77$ cm); the turbine solidity is $\sigma = N_b c/\pi D \approx 0.23$; and both the helical- and straight-bladed VAWTs rotate counterclockwise. For the helical-bladed VAWT, each blade is twisted counterclockwise from top to bottom with a constant rate of $4.5°$ per 1 cm vertical
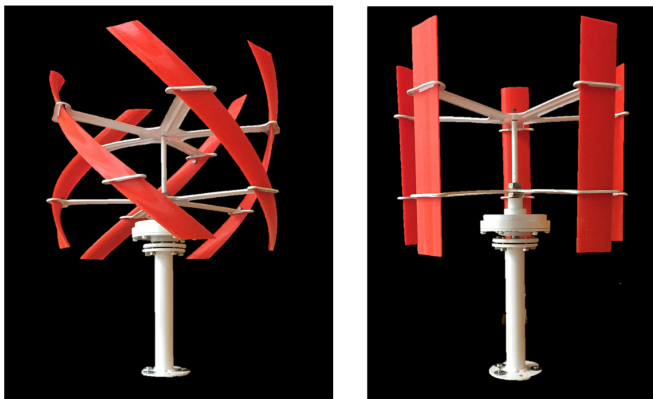
FIG. 1. Photos of VAWTs: (left panel) helical-bladed (H); (right panel) straight-bladed (S).

height, corresponding to a total twist angle of $\gamma = 135°$ between the top and bottom ends of each blade.

All the simulation cases reported in this study use identical inflow condition, which consists of a uniform mean inflow velocity of $U_0 = 13.0$ m/s and a homogeneous isotropic turbulence velocity fluctuation field with a turbulence intensity of $I_t = 0.02$. More details on the construction and implementation of the inflow condition are explained in Appendix B. Note that in Gharaati *et al.* [47] a turbulent boundary layer inflow condition was considered to study the performance of utility-scale VAWTs in open fields. In urban areas, small-size wind turbines often operate in complicated flow environments [78,79]. Investigating the effects of more realistic inflow conditions in urban environments requires considering specific turbine installation conditions case by case [80,81], which goes beyond the scope of the current study. Here we use the idealized uniform mean inflow condition similar to those considered in previous studies [24,38,40] and focus on studying the effects of VAWT blade geometry on the wake flow characteristics.

The corresponding turbine rotor Reynolds number is $\mathrm{Re}_D = U_0 D/\nu \approx 2.57 \times 10^5$, where the kinematic viscosity of air at $20\,°$C is $\nu = 1.52 \times 10^{-5}$ m^2/s. At this wind speed, the wind tunnel test showed that the helical-bladed VAWT spins freely at a TSR of $\lambda = R\Omega/U_0 \approx 0.6$, where Ω is the angular speed, and the straight-bladed VAWT spins freely at $\lambda \approx 0.7$. In order to isolate the effect of the blade geometry from other effects, we choose to prescribe an identical TSR of $\lambda = 0.6$ for both VAWTs so that their simulation results may be compared directly. The simulation cases with $\lambda = 0.6$ are the primary cases of our analysis. In addition, a lower TSR of $\lambda = 0.4$ is also chosen arbitrarily and considered for comparison purposes, at which the two VAWTs are expected to exhibit lower efficiency for energy production [23,45,82]. The corresponding blade chord Reynolds numbers for $\lambda = 0.6$ and 0.4 are $\mathrm{Re}_c = \lambda U_0 c/\nu \approx 2.21 \times 10^4$ and 1.47×10^4, respectively. At these relatively

TABLE I. Key parameters of VAWTs.

Number of blades (N_b)	5
Rotor radius (R)	0.15 m
Rotor diameter (D)	0.3 m
Rotor vertical height (H)	0.3 m
Blade cross section shape	NACA 0018 airfoil
Blade chord length (c)	4.3 cm
Blade thickness (t_b)	0.77 cm
Turbine solidity ($\sigma = N_b c/\pi D$)	0.23

TABLE II. Key parameters of the simulation cases.

Case	VAWT type	U_0 (m/s)	λ	Ω (rad/s)	$\mathrm{Re}_D = U_0 D/\nu$	$\mathrm{Re}_c = \lambda U_0 c/\nu$
S6	Straight	13.0	0.6	52.0	2.57×10^5	2.21×10^4
S4	Straight	13.0	0.4	34.7	2.57×10^5	1.47×10^4
H6	Helical	13.0	0.6	52.0	2.57×10^5	2.21×10^4
H4	Helical	13.0	0.4	34.7	2.57×10^5	1.47×10^4

low Reynolds numbers, the static lift and drag coefficients of the NACA0018 airfoil for ALM are adopted from Kumar *et al.* [83]. For the convenience of the discussion, each simulation case is named based on the blade shape and the TSR, e.g., "H6" for the helical-bladed VAWT rotating at $\lambda = 0.6$ and "S4" for the straight-bladed VAWT rotating at $\lambda = 0.4$. The key parameters of the simulation cases are summarized in Table II.

In all the reported simulation cases, the dimensions of the computational domain are $(L_x, L_y, L_z) = (4.5, 2.0, 2.0)$ m $= (30R, 13.33R, 13.33R)$. A fringe zone of length $L_{fr} = L_x/16$ is used for implementing the inflow–outflow condition, for which the technical details are given in Appendix B. The center of VAWT is located at $(x_0, y_0, z_0) = (0.5, 1, 1)$ m. The simulation domain is discretized using $N_x \times N_y \times N_z = 864 \times 384 \times 281$ grid points, yielding a grid resolution of $(\Delta x, \Delta y, \Delta z) \approx (0.0052, 0.0052, 0.0071)$ m. As shown in Appendix C, two additional test cases with identical physical parameters as case H4 are considered, one with a lower grid resolution (referred to as case H4-LR) and the other with a higher grid resolution (referred to as case H4-HR). The comparison of the time-averaged flow field obtained from these three simulations with different grid resolutions confirms that the spatial discretization using $N_x \times N_y \times N_z = 864 \times 384 \times 281$ grid points is sufficient for catching the flow physics. As explained in Appendix A, in the ALM the aerodynamic force induced by each VAWT blade element is smoothly distributed to the neighboring computational grid points using a Gaussian kernel function [57–60]. For the simulation cases listed in Table II, the width of the Gaussian kernel used in the ALM is $\epsilon = 0.02$ m. This kernel size yields $\epsilon/\Delta x \approx 3.8 > 2$, which ensures good numerical stability when applying the distributed turbine force to the LES model [57,58,84], and $\epsilon/c \approx 0.47$, which is close to the optimal kernel width criterion [$\epsilon/c \sim O(0.4)$] proposed by Martínez-Tossas *et al.* [85] based on potential flow theory analysis of flow past airfoil.

DNS data of 4.152 s duration extracted from JHTDB are used to generate the inflow condition based on the method described in Appendix B. Each simulation case uses a fixed time step of $\Delta t = 2.0 \times 10^{-5}$ s and has a total duration of 432 500 time steps, corresponding to 8.65 s. Simulation data after 17 300 time steps (i.e., after one flow through time of $L_x/U_0 \approx 0.346$ s) are used for the statistical analyses.

IV. RESULTS

In this section, the turbulent wake flows behind straight- and helical-bladed VAWTs are characterized and compared based on the LES results. Here one important effect of the blade geometry is illustrated in Fig. 2. As illustrated in Fig. 2(a) based on a uniform inflow (without turbulent fluctuation) and an analytical calculation using Eqs. (A1) and (A2), the force vector induced by one blade element exhibits considerable variation during one rotation cycle. The blade element induces more drag at rotation phases near $\theta = 0°$ and $\theta = 180°$ (see Fig. 24 for the definition of θ). As shown in Fig. 2(b) obtained from LES based on the turbulent inflow, each blade of the straight-bladed VAWT is located at one specific θ at an instant time of the rotation, resulting in similar aerodynamic forces at different vertical locations along the same blade but different force magnitudes and directions for different blades. In contrast, each twisted blade of the helical VAWT covers a wide range of θ (135°). As shown in Fig. 2(c), the corresponding aerodynamic force of each helical blade varies
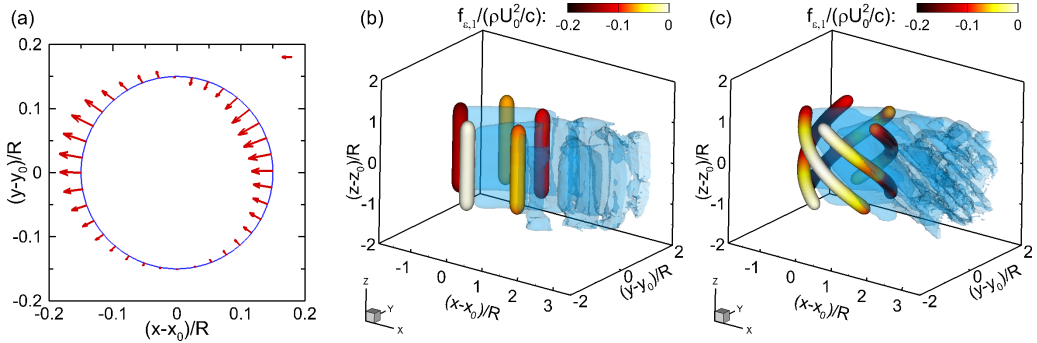
FIG. 2. (a) Illustration of the force vectors $\mathbf{F}_n$ at different azimuth angle θ. The reference vector shown on the top-right corner of (a) has a magnitude of $\rho U_0^2 c \Delta H / 2$. Panels (b) and (c) show the near-wake instantaneous flow structures for cases S6 and H6, respectively, visualized using the isosurfaces of $\widetilde{u} = 10$ m/s (in blue), and the instantaneous locations of the VAWT blades visualized using the isosurface of $G_b = 0.005$ and colored based on the local magnitude of the distributed streamwise force $f_{\epsilon,1}$. See Eq. (A14) in Appendix A for the definition of G_b.

continuously. In the following subsections, the effects of the blade geometry on the VAWT wake flow characteristics and wind power generation are investigated based on the LES data.

A. Instantaneous flow field

To illustrate the effects of the helical-shaped VAWT blades on the wake flow characteristics, first the instantaneous velocity fields obtained from the various LES cases are compared. Figure 3 shows the 3D visualizations of the wake flows behind the straight-bladed (case S6) and helical-bladed (case H6) VAWTs at $\lambda = 0.6$. The 3D wake structures are visualized using the isosurfaces of $\widetilde{u} = 10$ m/s,
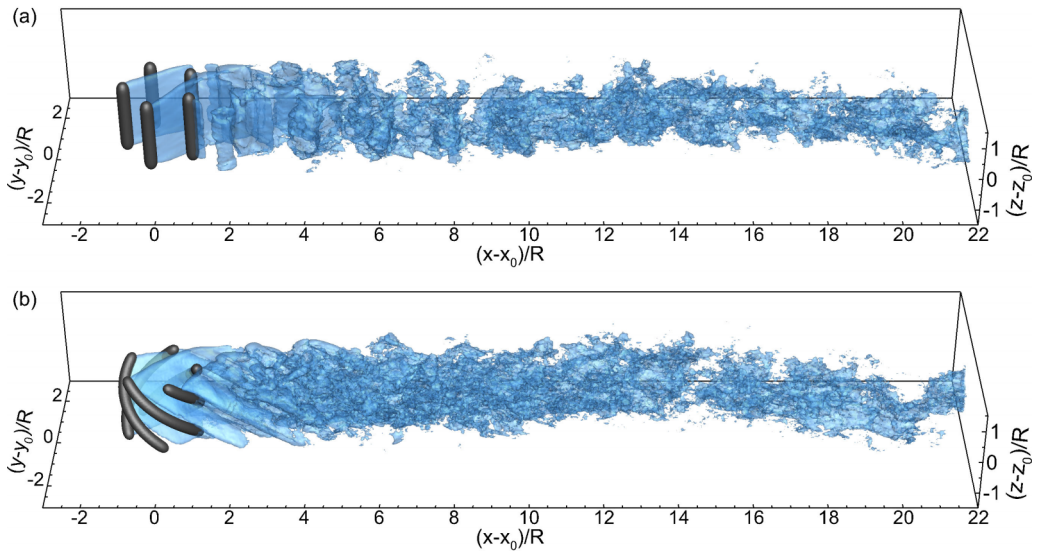

FIG. 3. Illustration of three-dimensional turbulent wake flows behind (a) straight-bladed (case S6) and (b) helical-bladed (case H6) VAWTs. The wake flow structures are visualized using the isosurfaces of $\widetilde{u} = 10$ m/s (in blue). The turbine blades are visualized using the isosurfaces of $G_b = 0.005$ (in black). See Eq. (A14) in Appendix A for the definition of G_b.
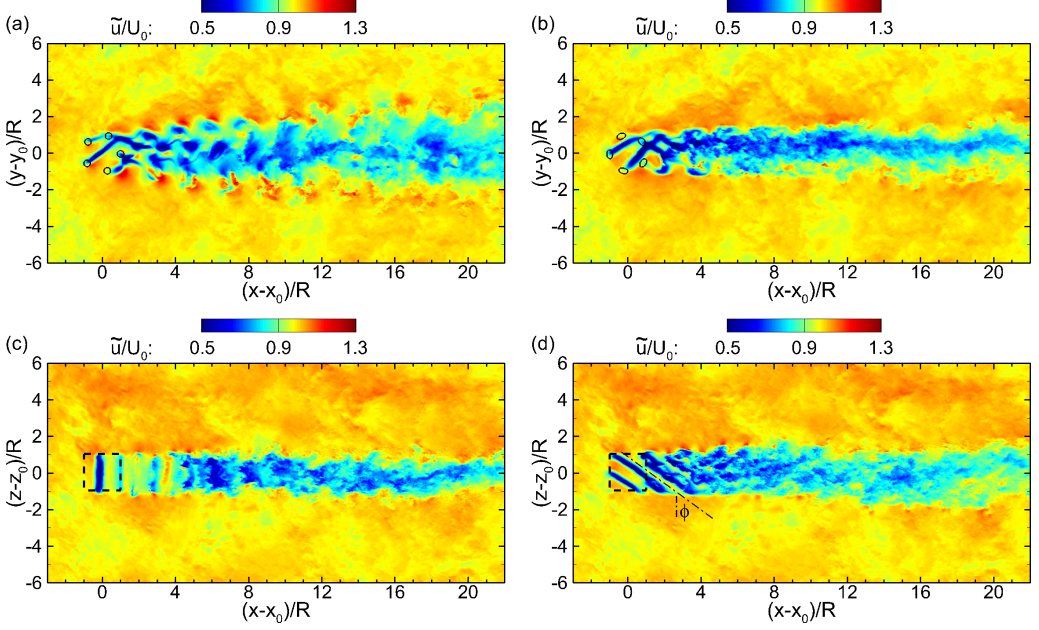
FIG. 4. Instantaneous streamwsie velocity $\widetilde{u}$ in flows past VAWTs rotating at $\lambda = 0.6$: (a), (c) straight-bladed VAWT (case S6); (b), (d) helical-bladed VAWT (case H6). The top-row panels (a), (b) show the (x, y) plane across the rotor center height (at $z = z_0$), and the bottom-row panels (c), (d) show the (x, z) plane across the rotor axis (at $y = y_0$). In (a) and (b), the instantaneous locations of VAWT blades are denoted by the isolines (solid lines) of $G_b = 0.005$. See Eq. (A14) in Appendix A for the definition of G_b. In (c) and (d), the VAWT rotor regions projected onto the (x, z) plane are enclosed by the dashed lines. In (d), the inclination angle of $\phi = 57.5°$ estimated based on Eq. (3) is denoted by the dash-dot lines.

corresponding to a velocity deficit of $\Delta \widetilde{u} = U_0 - \widetilde{u} = 3$ m/s. The corresponding 2D planar views of the velocity fields in cases S6 and H6 are shown in Figs. 4–6.

In the straight-bladed VAWT case S6 [Fig. 3(a)], the azimuth angle of rotation θ is synchronized for different sections of each straight blade. As a result, the wake flow structures (i.e., low-speed streaks) appear in the form of quasi-2D vertical sheets inside the rotor cylindrical region and in the near wake (at $x - x_0 \lesssim 4R$), where the blade-induced velocity fluctuations are primarily in the x and y directions. The quasi-2D (x, y)-plane flow motions in the near-wake region behind the straight-bladed VAWT can also been seen clearly from the planar views of the three velocity components $(\widetilde{u}, \widetilde{v}, \widetilde{w})$ as shown in Figs. 4–6. At $x - x_0 \lesssim 4R$, the contours of $\widetilde{u}$ and $\widetilde{v}$ show considerable fluctuations with organized vertical patterns on the (x, z) plane [see Figs. 4(a) and 4(c) and Figs. 5(a) and 5(c)], while the magnitude of $\widetilde{w}$ appears to be small in the near wake except in the two shear layers at $z - z_0 = \pm R$ [see Figs. 6(a) and 6(c)]. Further downstream in the far wake ($x - x_0 > 4R$), the quasi-2D wake flow structures break up into smaller 3D structures and the wake flow transitions to turbulence, which can be seen directly from the 3D visualization [Fig. 3(a)]. Consistently, the 2D velocity fields show that the magnitude of $\widetilde{w}$ [Fig. 6(c)] becomes comparable to that of $\widetilde{v}$ [Fig. 5(c)] at $x - x_0 > 4R$. Similar to the von Kármán vortex street in flow past a cylinder [86,87], the quasi-2D vortices generated by the several straight blades cause self-induced (x, y)-plane motions in the wake flow, resulting in noticeable spanwise expansion of the wake as it extends downstream [see Figs. 4(a) and 5(a)].

In contrast, in the helical-bladed VAWT case H6 [see Fig. 3(b)], the combined effects of the blade twist and turbine rotation result in a systematic shift of the azimuth angle θ for different sections of the same blade, i.e., there is a phase delay of θ from bottom to top for each blade during
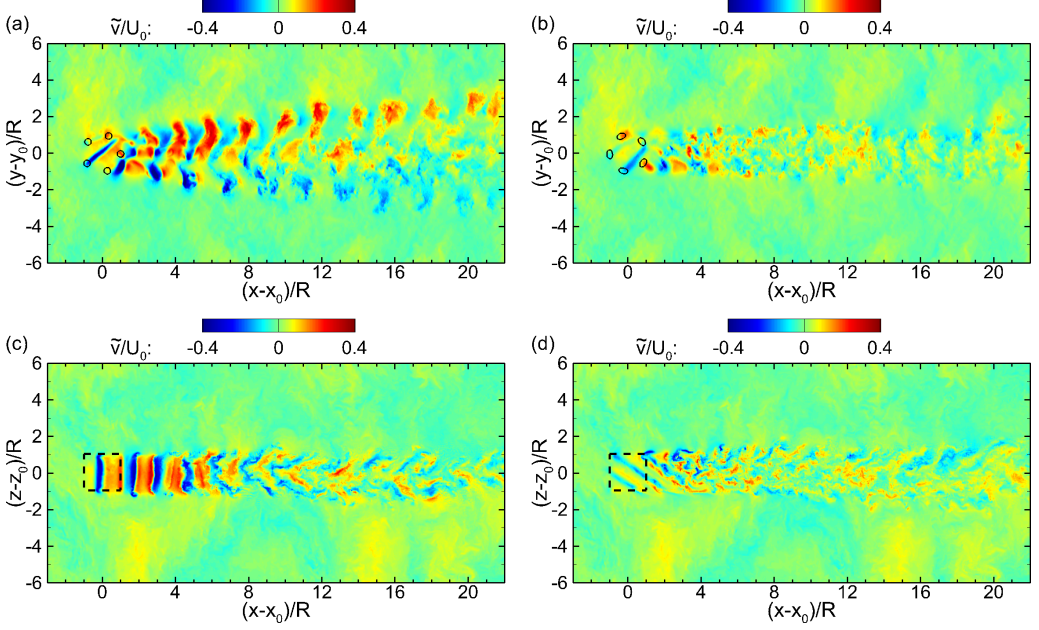
FIG. 5. Instantaneous spanwsie velocity $\widetilde{v}$ in flows past VAWTs rotating at $\lambda = 0.6$: (a), (c) straight-bladed VAWT (case S6); (b, d) helical-bladed VAWT (case H6). The top-row panels (a), (b) show the (x, y) plane across the rotor center height (at $z = z_0$), and the bottom-row panels (c), (d) show the (x, z) plane across the rotor axis (at $y = y_0$). In (a) and (b), the instantaneous locations of VAWT blades are denoted by the isolines (solid lines) of $G_b = 0.005$. See Eq. (A14) in Appendix A for the definition of G_b. In (c) and (d), the VAWT rotor regions projected onto the (x, z) plane are enclosed by the dashed lines.

the turbine rotation. Consequently, the low-speed streaks generated by the helical-shaped blades in case H6 exhibit many more 3D features than those in case S6. For example, the low-speed wake structures generated by different helical blades are inclined with respect to the vertical direction. This inclination can be seen clearly from the contours of $(\widetilde{u}, \widetilde{v}, \widetilde{w})$ near the turbine blades as shown in Figs. 4(d), 5(d), and 6(d). Take $\widetilde{u}$ in Fig. 4(d) as an example, and let ϕ be the inclination angle between the z direction and the low-speed streaks of $\widetilde{u}$ projected onto the (x, z) plane. By neglecting the effect of turbulent fluctuations, the value of ϕ can be estimated as

$$\phi = \arctan\left(\frac{aU_0}{\Omega/(\gamma/H)}\right) = \arctan\left(\frac{a\gamma R}{\lambda H}\right), \tag{3}$$

where a is a factor accounting for the reduction of the streamwise advection speed of the blade wakes relative to the mean inflow speed U_0. For case H6, an estimated value of $a \approx 0.8$ [based on the time-averaged streamwise velocity in the near wake; see Figs. 10(b) and 10(d) in Sec. IV B] yields $\phi \approx 57.5°$ [shown by the dash-dot lines in Fig. 4(d)], which is very close to the inclination angle observed directly from the LES results. If a lower TSR is used (e.g., case H4 with $\lambda = 0.4$), the inclination angle ϕ is expected to increase as shown by Eq. (3).

In case H6, the helical blades located on the downstream side of the turbine rotor also have more chance to cut through the low-speed streaks generated by the upstream blades, inducing more disturbances to the low-speed flow sheets to trigger the transition of the wake toward the turbulent state. As shown in Fig. 3(b), in case H6 the velocity isosurfaces already show the sign of turbulence at $x - x_0 \approx 2R$. The helical-bladed VAWT generates highly 3D flow motions in the wake, as shown by the fluctuations of the three velocity components with comparable magnitudes [see Figs. 4(b), 4(d), 5(b), 5(d), 6(b), 6(d)]. Without the quasi-2D von Kármán vortex street wake flow pattern like in
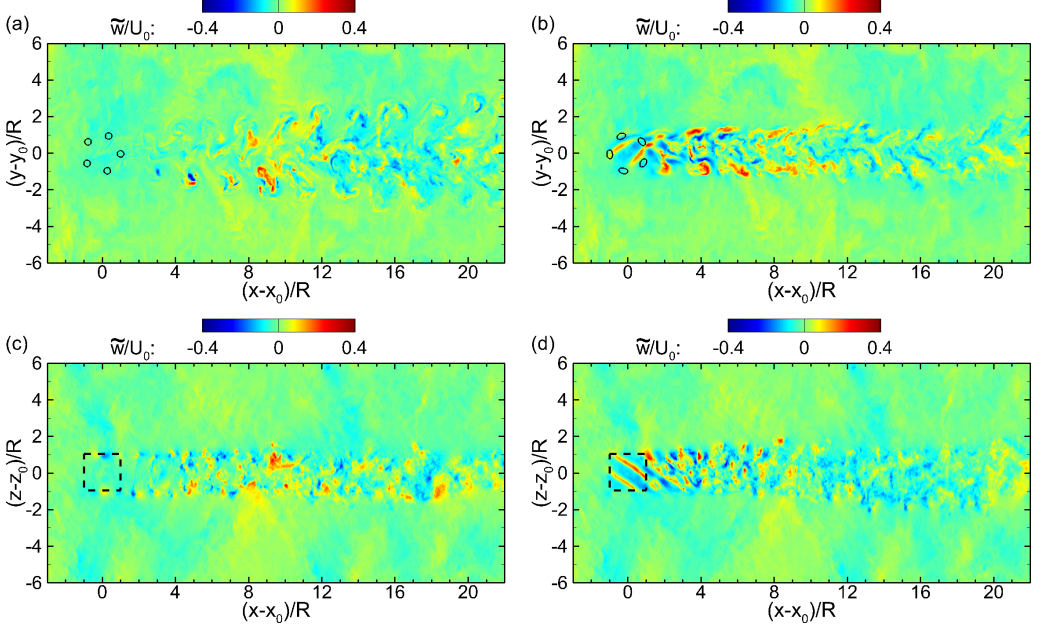
FIG. 6. Instantaneous vertical velocity $\widetilde{w}$ in flows past VAWTs rotating at $\lambda = 0.6$: (a), (c) straight-bladed VAWT (case S6); (b), (d) helical-bladed VAWT (case H6). The top-row panels (a), (b) show the (x, y) plane across the rotor center height (at $z = z_0$), and the bottom-row panels (c), (d) show the (x, z) plane across the rotor axis (at $y = y_0$). In (a) and (b), the instantaneous locations of VAWT blades are denoted by the isolines (solid lines) of $G_b = 0.005$. See Eq. (A14) in Appendix A for the definition of G_b. In (c) and (d), the VAWT rotor regions projected onto the (x, z) plane are enclosed by the dashed lines.

case S6, the wake flow of the helical-bladed VAWT in case H6 does not exhibit significant spanwise expansion towards the downstream.

B. Time-averaged velocity fields

Time-average statistics of the wake flows are calculated based on 8304 instantaneous snapshots sampled between $t = 0.346\,\mathrm{s}$ and $8.65\,\mathrm{s}$ (corresponding to 67 full rotation cycles for $\lambda = 0.6$ and 47 cycles for $\lambda = 0.4$), with a fixed sampling time interval of $0.001\,\mathrm{s}$ (i.e., one sample per every 50 simulation time steps). Note that the period for one VAWT rotation is about $0.121\,\mathrm{s}$ for $\lambda = 0.6$ and about $0.181\,\mathrm{s}$ for $\lambda = 0.4$. The current time-average sampling interval is sufficiently small to ensure that the near-wake flow unsteadiness related to the rotation phase of the VAWT gets averaged out smoothly. Hereinafter, $\overline{f}$ denotes the time average of a physical quantity $\widetilde{f}$ resolved by LES, and $f' = \widetilde{f} - \overline{f}$ denotes the corresponding temporal fluctuation.

As shown by the instantaneous flow fields in Sec. IV A, different blade shapes can generate distinct differences in the 3D characteristics of the wake flow. The differences are also reflected in the time-averaged velocity fields. Figure 7 compares the time-averaged spanwise velocity $\overline{v}$ on the (x, y) plane at $z = z_0$ in cases S6 and H6, and Fig. 8 compares the corresponding time-averaged vertical velocity $\overline{w}$. In the straight-bladed VAWT case S6, the mean wake flow is dominated by the spanwise expansion of the wake, as indicated by the high magnitude of $\overline{v}$ in Fig. 7(a) and the low magnitude of $\overline{w}$ in Fig. 8(a). Figure 9(a) shows the corresponding (y, z)-plane view of $\overline{v}$ at $x - x_0 = 8R$ for case S6. On the $y - y_0 < 0$ side (i.e., the left half in Fig. 9(a)), the mean flow motion along the $-y$ direction generates a pair of counter-rotating streamwise vortices $\mathrm{L_n}$ and $\mathrm{L_p}$. In particular, $\mathrm{L_n}$ has a negative mean streamwise vorticity $\overline{\omega}_x < 0$ and $\mathrm{L_p}$ has a positive mean
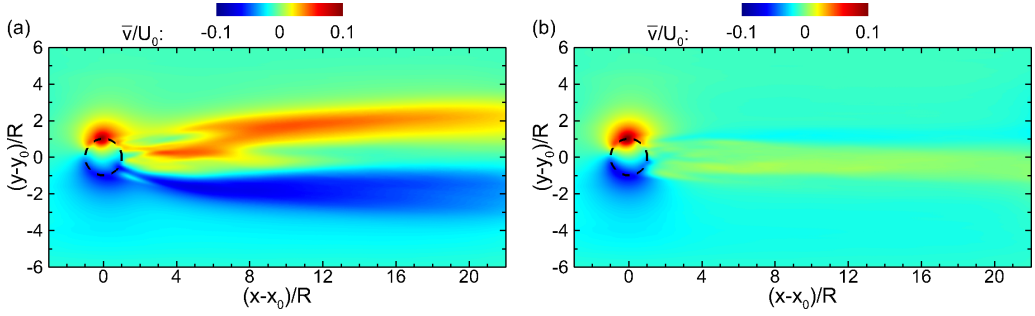
FIG. 7. Time-averaged spanwsie velocity $\overline{v}$ in flows past straight- and helical-bladed VAWTs rotating at $\lambda = 0.6$: (a) case S6; (b) case H6. The (x, y) plane at $z = z_0$ is shown, with the rotor region denoted by the dashed-line circle.
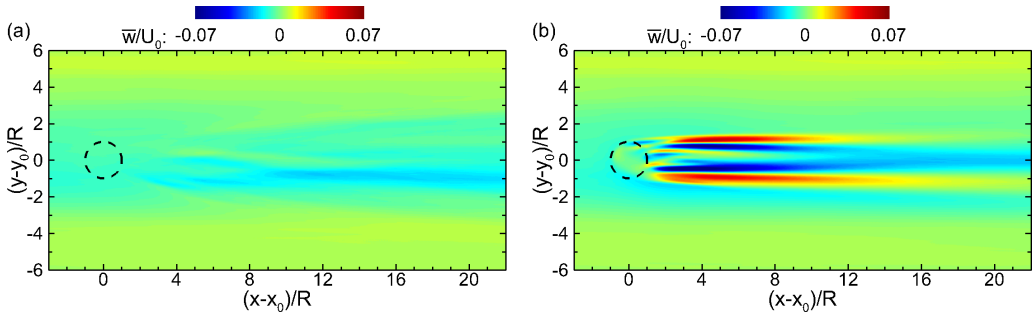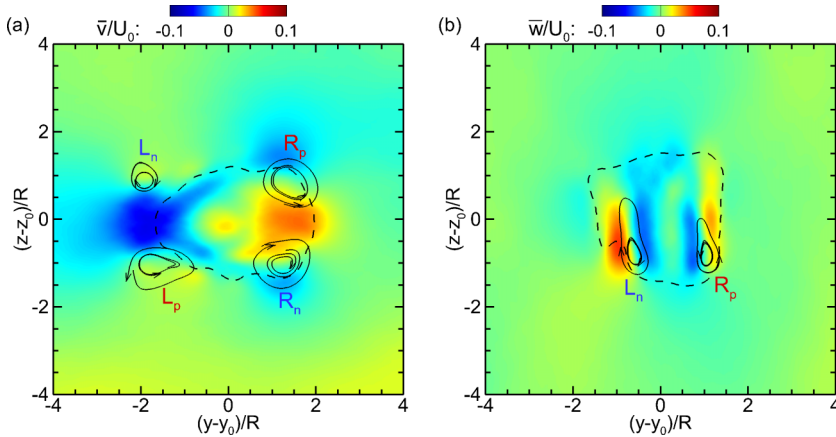

FIG. 8. Time-averaged vertical velocity $\overline{w}$ in flows past straight- and helical-bladed VAWTs rotating at $\lambda = 0.6$: (a) case S6; (b) case H6. The (x, y) plane at $z = z_0$ is shown, with the rotor region denoted by the dashed-line circle.

FIG. 9. Time-averaged velocity fields on the (y, z) plane at $x - x_0 = 8R$. Panel (a) shows the color contours of $\overline{v}$ for case S6. Panel (b) shows the color contours of $\overline{w}$ for case H6. In each panel, the dashed isoline of $\overline{u}/U_0 = 0.98$ is used to highlight the wake region. The primary vortices associated with the mean wake flow motions on the (y, z) plane are highlighted by the 2D streamlines based on $(\overline{v}, \overline{w})$, and labeled based on the relative location ("L" for left and "R" for right) and the sign of the vorticity $\overline{\omega}_x$ (subscript "p" for positive $\overline{\omega}_x$ and "n" for negative $\overline{\omega}_x$).
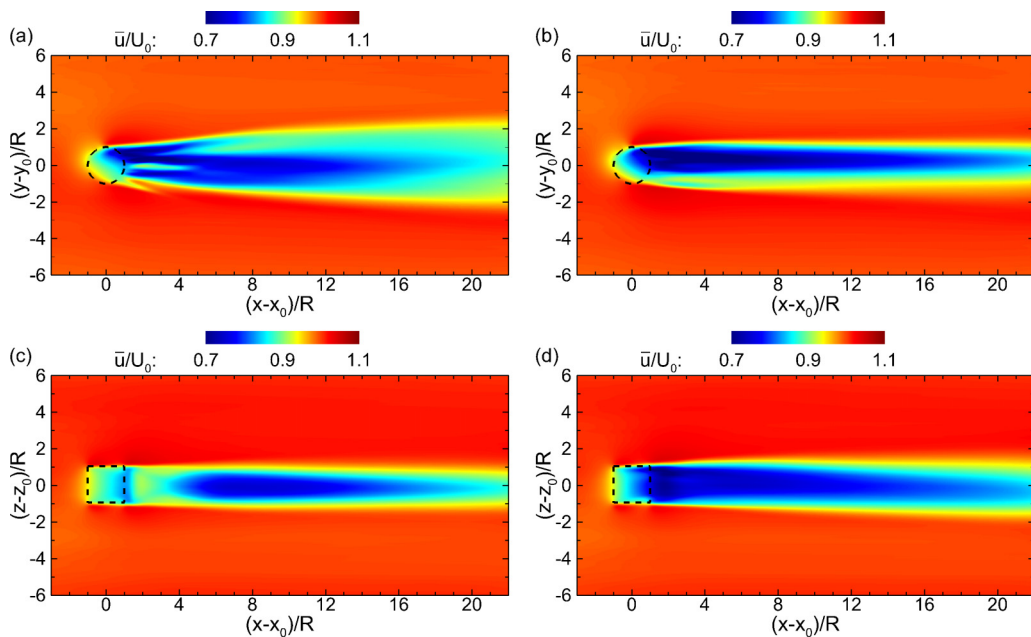
FIG. 10. Time-averaged streamwsie velocity $\bar{u}$ in flows past VAWTs rotating at $\lambda = 0.6$: (a), (c) straight-bladed VAWT (case S6); (b), (d) helical-bladed VAWT (case H6). The top-row panels (a), (b) show the (x, y) plane across the rotor center height (at $z = z_0$) and the bottom-row panels (c), (d) show the (x, z) plane across the rotor axis (at $y = y_0$). In each panel, the VAWT rotor region is denoted by the dashed lines.

streamwise vorticity $\bar{\omega}_x > 0$, as indicated by the local 2D streamline patterns of the mean velocities $(\bar{v}, \bar{w})$. Similarly, on the $y - y_0 > 0$ side [i.e., the right half in Fig. 9(a)], the mean spanwise flow motion along the $+y$ direction generates another pair of counter-rotating streamwise vorticies R_p and R_n, which have opposite rotating directions as L_n and L_p, respectively. The (y, z)-plane mean flow pattern in case H6 is very different from that in case S6. As shown in Fig. 8(b), the rotating helical-shaped blades generate two regions with mean upward flows near $y - y_0 = \pm R$, which are accompanied by two downward flow regions on the inner sides of the turbine wake. Blade-induced vertical flow motions have also been reported in previous studies of flows past helical-bladed VAWTs at higher TSRs [29,46,47]. For the current helical-bladed VAWT illustrated in Fig. 3(b), the bottom end of each blade cuts underneath the flow and lift it along the inclined blade surface when rotating counterclockwise, which is similar to the effect of a screwdriver. Associated with the upward-downward counter flow motions, there are two primary mean streamwise vorticies L_n and R_p as shown in Fig. 9(b).

The differences in the mean (y, z)-plane flow motions in cases S6 and H6 cause the wake flows in these two cases to develop differently towards the downstream. Figure 10 shows the (x, y)- and (x, z)-plane views of the mean streamwise velocity $\bar{u}$ for cases S6 and H6, and Fig. 11 shows the corresponding $\bar{u}$ contours on the (y, z) planes at three different streamwise locations. In case S6, the wake expands mainly in the spanwise direction. The counter-rotating motions of vorticies L_n and R_p induce downward flows in between; similarly, upward flows are generated between L_p and R_n. These inward mean flows suppress the vertical expansion of the wake in case S6, which can be seen in Figs. 10(c) and 11(a). In contrast, the vertical counter-flow motions in case H6 [see Fig. 9(b)] cause the wake of the helical-bladed VAWT to mainly expand in the vertical direction, which is shown clearly in Fig. 11(b).

In the near-wake region (at $x - x_0 \lesssim 4R$) of case S6 [see Fig. 10(a)], the contours of $\bar{u}$ show three distinct low-speed streaks, corresponding to the three streets of instantaneous velocity deficit
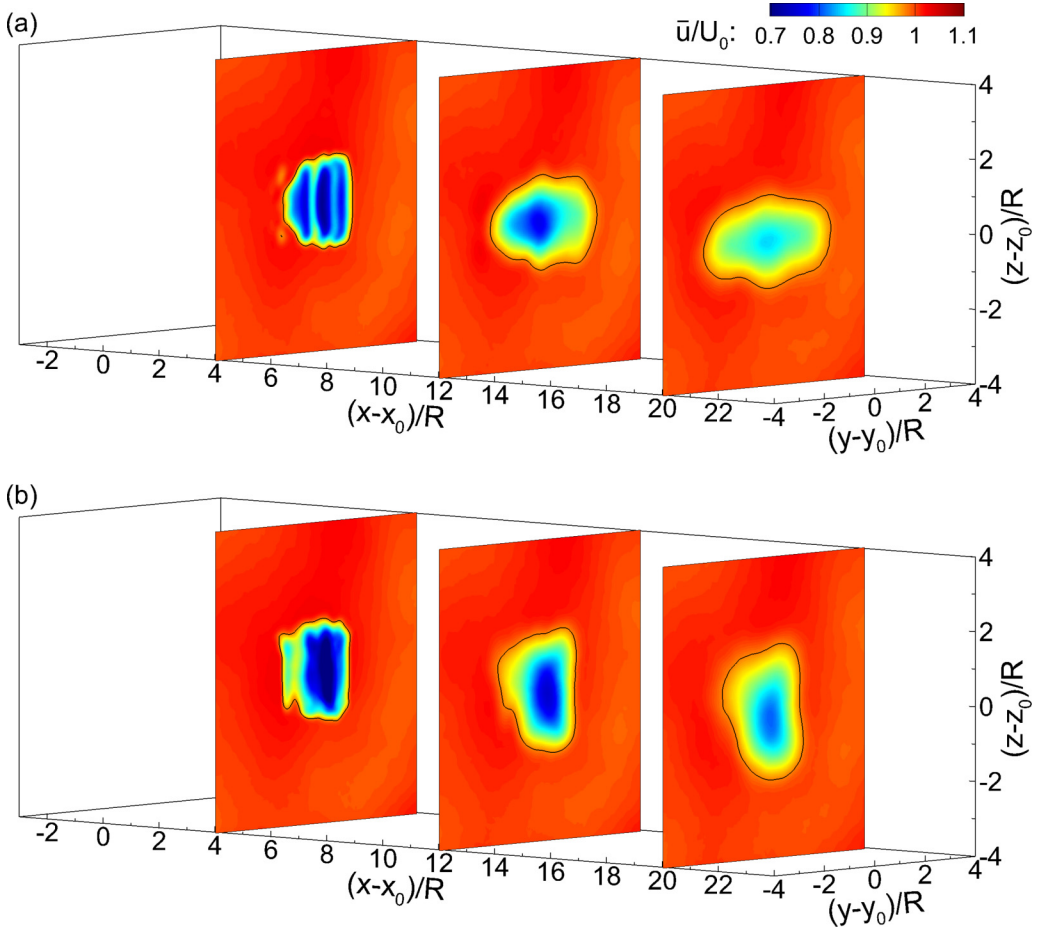
FIG. 11. Time-averaged streamwsie velocity $\bar{u}$ in flows past VAWTs rotating at $\lambda = 0.6$: (a) straight-bladed VAWT (case S6); (b) helical-bladed VAWT (case H6). The contours of $\bar{u}/U_0$ are shown on three representative (y, z) planes at $x - x_0 = 4R$, $12R$ and $20R$. On each plane, the solid isoline of $\bar{u}/U_0 = 0.98$ is used to highlight the edge of the wake region.

structures shedding from the straight VAWT blades that can be seen in Fig. 4(a). These low-speed streaks are not well blended because the flow structures are still in the form of organized 2D vertical sheets in the near wake [see Fig. 3(a)], which do not provide sufficient mixing. At $x - x_0 > 4R$, the wake flow transitions to turbulence and the contours of $\bar{u}$ become much smoother along the spanwise direction due to turbulent mixing. Note that $\bar{u}$ shown in Fig. 10(c) does not appear to have significant deficit in the near wake at $x - x_0 \lesssim 4R$. This is because Fig. 10(c) shows the (x, z) plane at $y = y_0$, which coincides with the spanwise location of the narrow gap between two low-speed streaks shown in Fig. 10(a) (i.e., the narrow region at $x - x_0 = 1R \sim 4R$ around $y = y_0$).

For wind energy harvesting, wind turbines are often deployed in the form of large arrays. The wind speed recovery of the turbine wake is crucial for the overall performance of the turbine array. Using the time-averaged velocity at the inflow boundary as the reference, the turbine-induced mean streamwise velocity deficit can be calculated as $\Delta\bar{u}(x, y, z) = \bar{u}(0, y, z) - \bar{u}(x, y, z)$. Because $\bar{u}(0, y, z)$ is identical in all the simulation cases, the differences exhibited in $\Delta\bar{u}$ are expected to be due to the blade geometry. Figure 12 shows the spanwise profiles of $\Delta\bar{u}$ at $z = z_0$ and different streamwise locations for cases S6 and H6, and Fig. 13 shows the corresponding vertical profiles
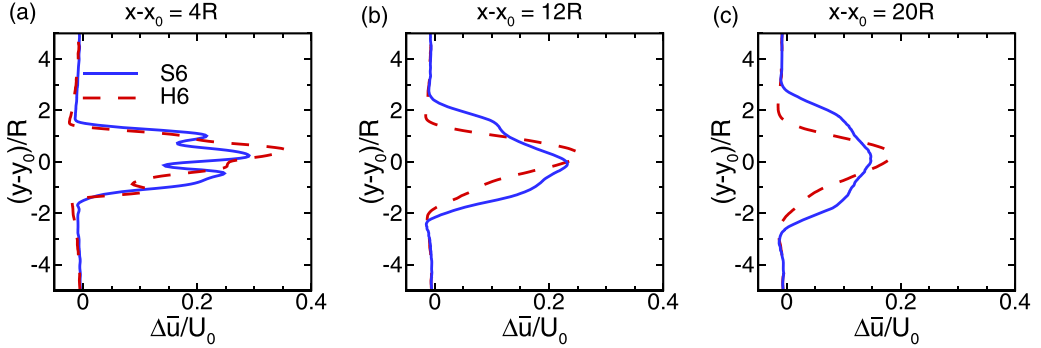
FIG. 12. Spanwise profiles of mean streamwise velocity deficit $\Delta\bar{u}$ for cases S6 (solid lines) and H6 (dashed lines). The profiles are extracted from the (x, y) plane of $z = z_0$ at different streamwise locations $x - x_0 =$ (a) $4R$, (b) $12R$, and (c) $20R$.

at $y = y_0$. In the near-wake region at $x - x_0 = 4R$, Fig. 13(a) shows that the vertical profile of $\Delta\bar{u}$ for case S6 has a noticeably lower peak value than that for case H6. It should be noted that this lower peak value of the $\Delta\bar{u}(z)$ profile at $x - x_0 = 4R$ is because the spanwise location where the profile is extracted ($y = y_0$) coincides with the location of low-$\Delta\bar{u}$ streak, which can be seen clearly in Figs. 10(a), 11(a), and 12(a). It is a local feature in the near-wake region of case S6 and does not indicate that the straight-bladed VAWT in case S6 generates less velocity deficit than the helical-bladed VAWT in case H6. Overall, the wake of case H6 exhibits comparable velocity recovery along the center line [(y_0, z_0)] as that of case S6, but with much narrower spanwise width, e.g., about $4R$ in case H6 versus about $6R$ in case S6 at $x - x_0 = 20R$. The difference in the vertical width of the wake along the center (at $y = y_0$) in these two cases is less significant, with the H6 case exhibiting slightly wider vertical extension of the wake than that in case S6. Note that one commonly considered strategy for improving the wind farm performance is to deploy turbines in staggered array pattern in order to avoid the impacts of the upstream turbine wakes to the downstream ones [26,88–90]. The simulation results in Fig. 12 suggest that for VAWTs operating at relatively low TSRs, using the helical-bladed VAWT design may increase the chance for the downstream VAWTs to avoid the relatively narrow wakes of the upstream VAWTs, which may improve the overall performance of the VAWTs array. Note that reduced-order wake models [91,92] have been developed and used as cost efficient tools for designing wind farms. They rely on information such as wake expansion rate in order to model the downstream development of the
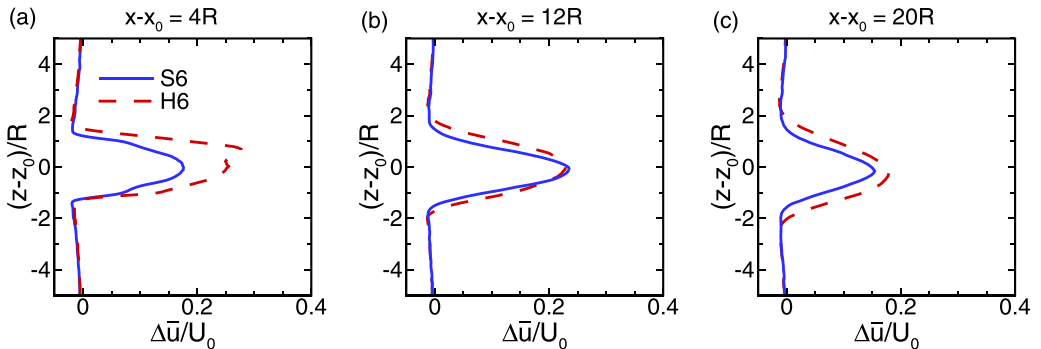

FIG. 13. Vertical profiles of mean streamwise velocity deficit $\Delta\bar{u}$ for cases S6 (solid lines) and H6 (dashed lines). The profiles are extracted from the (x, z) plane of $y = y_0$ at different streamwise locations $x - x_0 =$ (a) $4R$, (b) $12R$, and (c) $20R$.
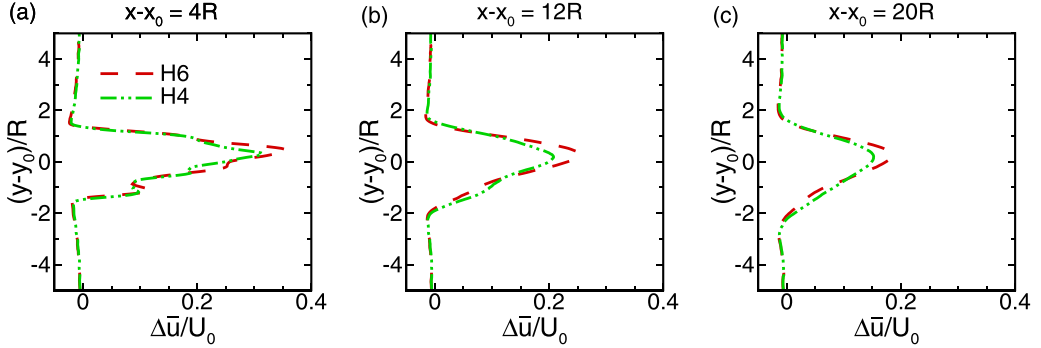
FIG. 14. Spanwise profiles of mean streamwise velocity deficit $\Delta\overline{u}$ for cases H6 (dashed lines) and H4 (dot dot dashed lines). The profiles are extracted from the (x, y) plane of $z = z_0$ at different streamwise locations $x - x_0 =$ (a) $4R$, (b) $12R$, and (c) $20R$.

wake. The results shown above suggest that it may be necessary to take into account blade geometry effect when developing reduced-order model for VAWTs.

Figures 14 and 15 compare the spanwise and vertical profiles of $\Delta\overline{u}$ for cases H6 and H4. When the TSR is reduced to $\lambda = 0.4$, the profiles of $\Delta\overline{u}$ appear to have similar shapes as those for $\lambda = 0.6$, but with smaller magnitudes. This comparison suggests that the effects of the helical-shaped blades on the wake flow characteristics are qualitatively similar at $\lambda = 0.4$ and 0.6.

Because the helical-bladed VAWT considered in this study spins freely at $\lambda = 0.6$ (see Sec. III), we do not include other simulation cases with higher TSR. For comparison, Gharaati et $al.$ [47] simulated VAWT wake flows for a higher TSR of $\lambda = 1.19$. Different from cases S6 and H6 reported in this study (see Figs. 10–13), the helical- and straight-bladed VAWTs with $\lambda = 1.19$ generated wake flows with similar spanwise and vertical widths; for the straight-bladed VAWT, the mean streamwise velocity contours in the near-wake region also appear to be much smoother at $\lambda = 1.19$ (see Figs. 13–15 in Ref. [47]) than at $\lambda = 0.6$ due to the more significant stirring effects induced by faster rotating blades. Note that the VAWTs considered in Gharaati et $al.$ [47] have different parameters from the VAWTs considered in this study. Thus the comparison discussed here should be regarded as qualitative rather than quantitative.
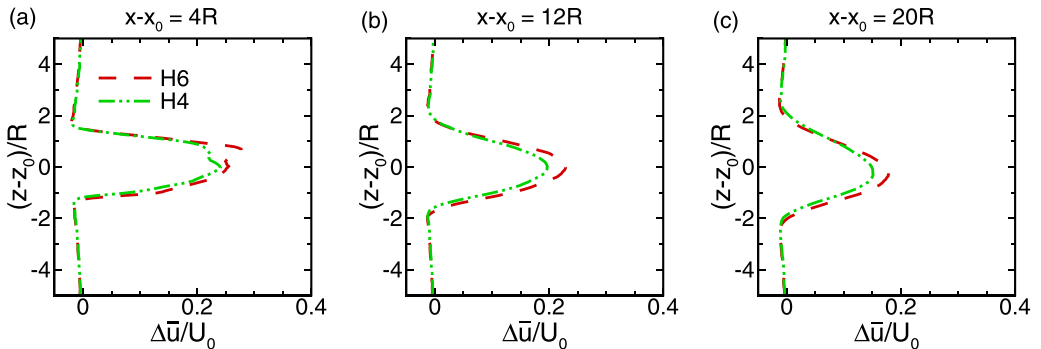

FIG. 15. Vertical profiles of mean streamwise velocity deficit $\Delta\overline{u}$ for cases H6 (dashed lines) and H4 (dot dot dashed lines). The profiles are extracted from the (x, y) plane of $z = z_0$ at different streamwise locations $x - x_0 =$ (a) $4R$, (b) $12R$, and (c) $20R$.
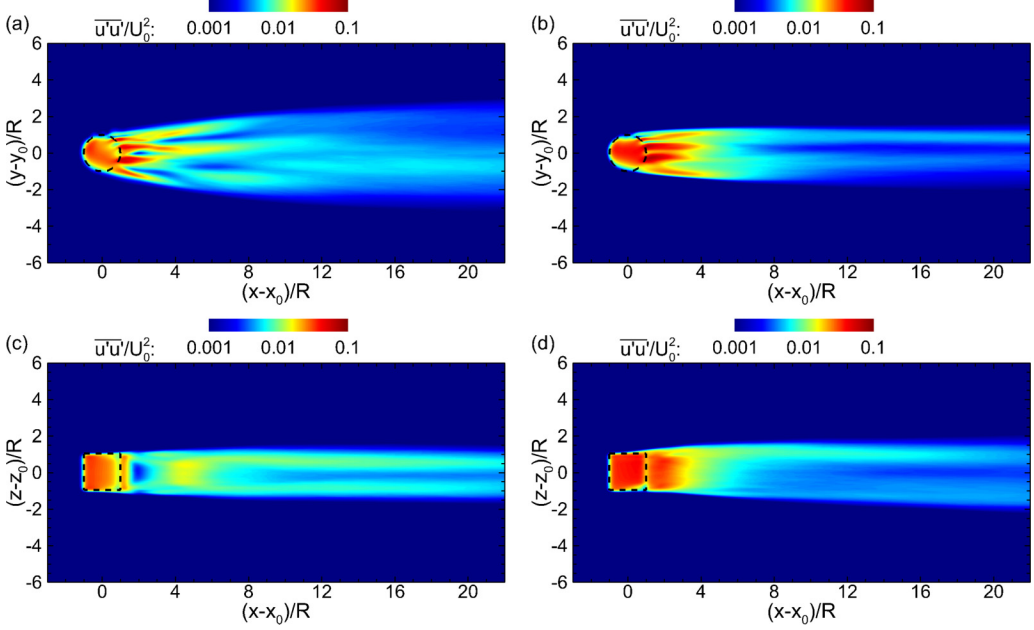
FIG. 16. Streamwise velocity variance $\overline{u'u'}$ in flows past VAWTs rotating at $\lambda = 0.6$: (a), (c) straight-bladed VAWT (case S6); (b), (d) helical-bladed VAWT (case H6). The top-row panels (a), (b) show the (x, y) plane across the rotor center height (at $z = z_0$), and the bottom-row panels (c), (d) show the (x, z) plane across the rotor axis (at $y = y_0$). In each panel, the VAWT rotor region is denoted by the dashed lines.

C. Time-averaged statistics of velocity fluctuations

In addition to the effects on the mean velocity field, the shape of the VAWT blade also affects the turbulent characteristics of the wake flow. Figures 16–18 show the 2D views of the velocity variances $\overline{u'u'}$, $\overline{v'v'}$, and $\overline{w'w'}$, respectively, for cases S6 and H6.

In the straight-bladed VAWT case S6, $\overline{u'u'}$ in Figs. 16(a) and 16(c) and $\overline{v'v'}$ in Figs. 17(a) and 17(c) exhibit high values within the rotor region and in the near wake (at $x - x_0 \lesssim 4R$), where the velocity fluctuations are dominated by the quasilaminar quasi-2D unsteady flow motions in the (x, y) plane induced by the rotating straight blades as illustrated in Fig. 3(a). In the same near-turbine region, $\overline{w'w'}$ shown in Figs. 18(a) and 18(c) appears to be negligible due to the quasi-2D motions, except in the two shear layers at around $z - z_0 = \pm R$ [see Fig. 18(c)]. Further downstream ($x - x_0 > 4R$), the wake flow transitions to 3D turbulence, resulting in more vertical fluctuations [Figs. 18(a) and (18c)]. In contrast, the helical-bladed VAWT case H6 exhibits comparable magnitudes for the spanwise velocity variance $\overline{v'v'}$ [Figs. 17(b) and 17(d)] and the vertical velocity variance $\overline{w'w'}$ [Figs. 18(b) and 18(d)] in the near-wake region because of the 3D characteristics of the helical-bladed VAWT wake. The wake flow in case H6 exhibits weaker $\overline{v'v'}$ but stronger $\overline{w'w'}$ than that in case S6. The streamwise velocity variance $\overline{u'u'}$ in the near wake of case H6 also appears to be stronger than that in case S6.

Combining the three velocity fluctuation components together, $\overline{k} = (\overline{u'u'} + \overline{v'v'} + \overline{w'w'})/2$ measures the overall fluctuation level of the wake flow. For simplification, we refer to $\overline{k}$ as the time-averaged turbulent kinetic energy (TKE) even though the velocity fluctuations close to the VAWT rotor region are dominated by quasilaminar unsteady wake oscillations rather than turbulence. Figure 19 compares the (x, y) and (x, z) planar distributions of $\overline{k}$ for cases S6 and H6, and Fig. 20 compares the (y, z) planar distributions of $\overline{k}$ at three different streamwise locations. Cases S6 and H6 exhibit similar magnitudes of $\overline{k}$ in the near-wake region. Towards downstream, the region of
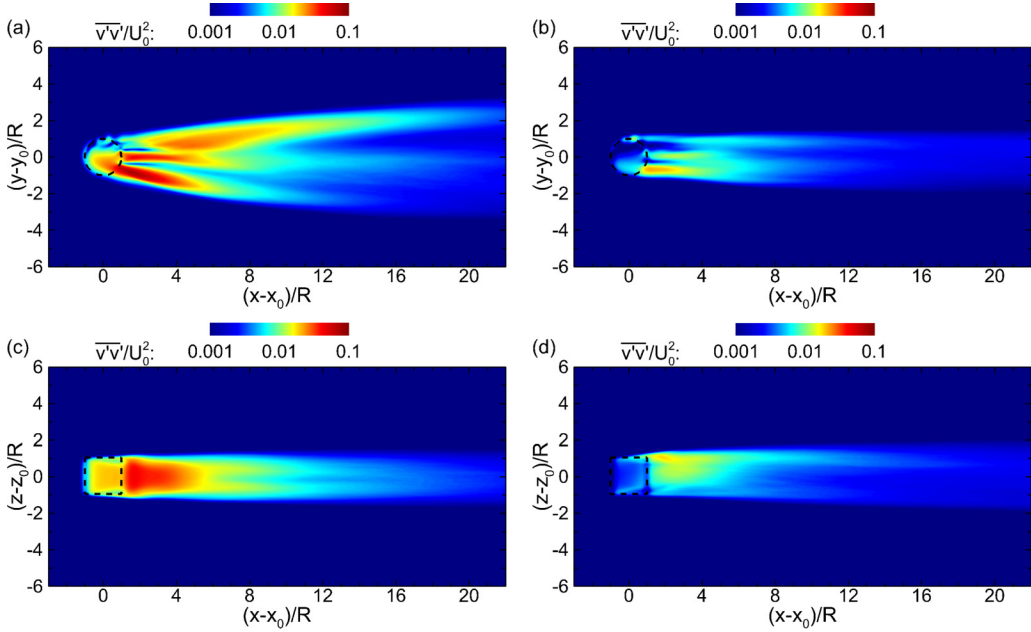
FIG. 17. Spanwise velocity variance $\overline{v'v'}$ in flows past VAWTs rotating at $\lambda = 0.6$: (a), (c) straight-bladed VAWT (case S6); (b), (d) helical-bladed VAWT (case H6). The top-row panels (a), (b) show the (x, y) plane across the rotor center height (at $z = z_0$), and the bottom-row panels (c), (d) show the (x, z) plane across the rotor axis (at $y = y_0$). In each panel, the VAWT rotor region is denoted by the dashed lines.
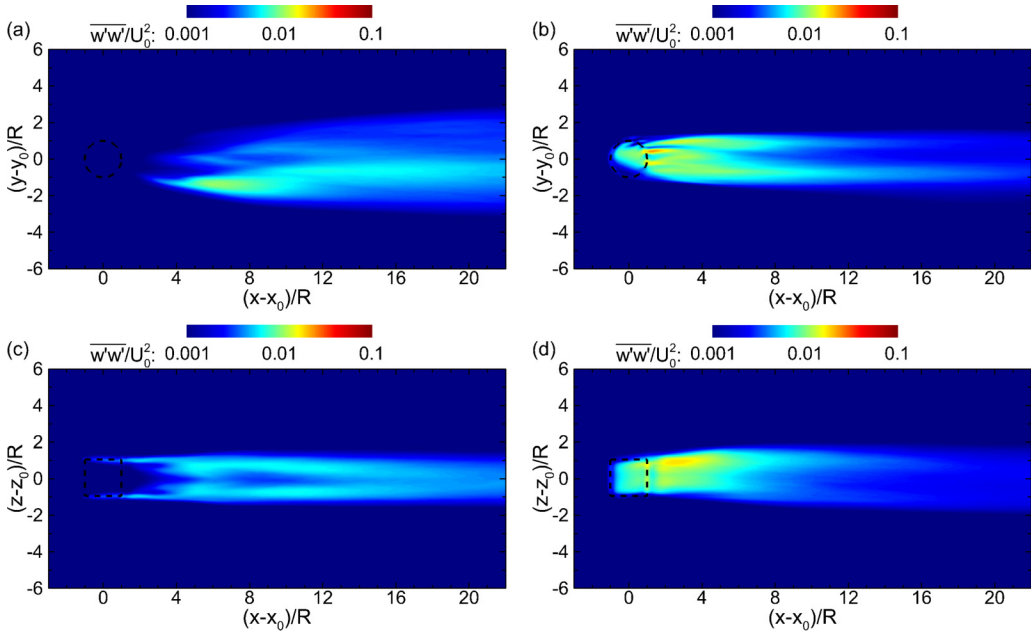

FIG. 18. Vertical velocity variance $\overline{w'w'}$ in flows past VAWTs rotating at $\lambda = 0.6$: (a), (c) straight-bladed VAWT (case S6); (b), (d) helical-bladed VAWT (case H6). The top-row panels (a), (b) show the (x, y) plane across the rotor center height (at $z = z_0$), and the bottom-row panels (c), (d) show the (x, z) plane across the rotor axis (at $y = y_0$). In each panel, the VAWT rotor region is denoted by the dashed lines.
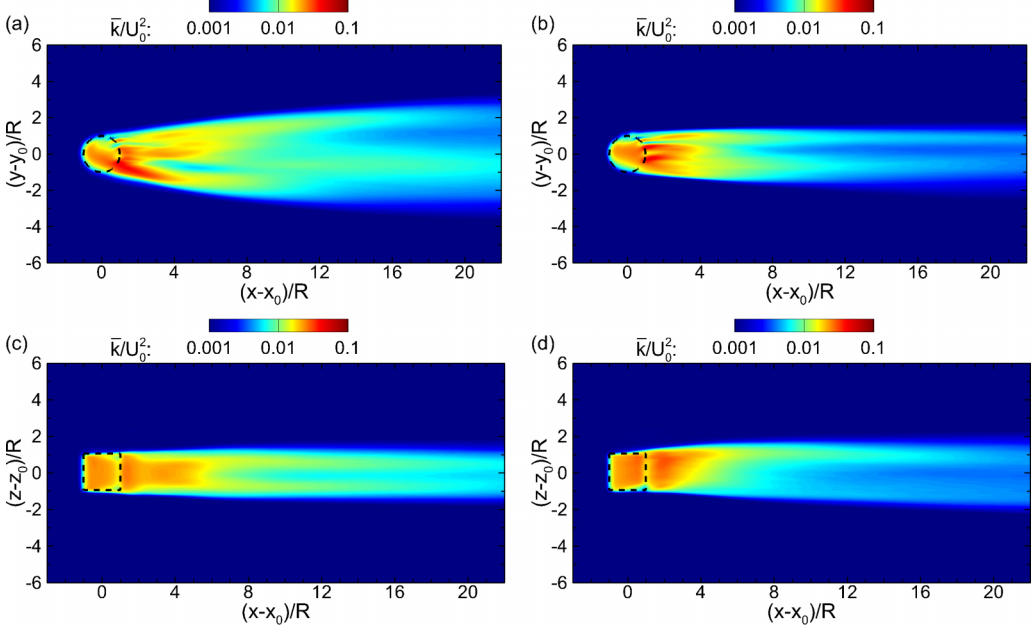
FIG. 19. Time-averaged TKE $\bar{k} = (\overline{u'u'} + \overline{v'v'} + \overline{w'w'})/2$ in flows past VAWTs rotating at $\lambda = 0.6$: (a), (c) straight-bladed VAWT (case S6); (b), (d) helical-bladed VAWT (case H6). The top-row panels (a), (b) show the (x, y) plane across the rotor center height (at $z = z_0$), and the bottom-row panels (c), (d) show the (x, z) plane across the rotor axis (at $y = y_0$). In each panel, the VAWT rotor region is denoted by the dashed lines.

high turbulence intensity in case S6 expands considerably in the spanwise direction with negligible expansion in the vertical direction [Figs. 19(a), 19(c), and 20(a)]; in case H6, the high turbulence intensity region expands slightly in the vertical direction, with negligible expansion in the spanwise direction [Figs. 19(b), 19(d), and 20(b)].

Because $\bar{k}$ consists of contributions from both quasi-laminar unsteady fluctuations caused by rotating VAWT blades and true turbulent fluctuations, here the SGS kinetic energy dissipation is used to help identify the regions dominated by turbulent fluctuations. The time-averaged SGS kinetic energy dissipation is defined as $\overline{\varepsilon}_{sgs} = \overline{\nu_{sgs} \frac{\partial \widetilde{u}_i}{\partial x_j} \frac{\partial \widetilde{u}_i}{\partial x_j}}$. It represents the kinetic energy cascade from the LES resolved grid scale to unresolved subgrid scales [93–95]. Flow regions with more turbulence motions are expected to have high values of $\overline{\varepsilon}_{sgs}$, as shown in Fig. 21. In case S6, $\overline{\varepsilon}_{sgs}$ exhibits much stronger correlation with $\overline{w'w'}$ than with $\overline{u'u'}$ and $\overline{v'v'}$, and the low SGS dissipation in the near wake confirms the dominance of quasilaminar wake flow motions there. Compared with case S6, case H6 shows much higher SGS dissipation in the VAWT wake at $x - x_0 \lesssim 12R$, suggesting that the more 3D turbulent flow structures in the wake behind helical-bladed VAWT help promote the transition to turbulence and enhance the decay of turbulence intensity of the wake.

Note that in the higher TSR cases (i.e., $\lambda = 1.19$) reported in Gharaati *et al.* [47], the helical-bladed VAWTs affect the turbulence statistics by inducing a noticeable vertical tilting of the wake. For example, in their helical VAWT case with similar blade twist direction as the current case H6, the faster rotating helical blades induce mean vertical flow motions that tilt the central region of the VAWT wake upward [29,47], which increases the velocity shear and enhances the turbulence intensity in the shear layer at the upper edge of the VAWT wake. Unlike the significant difference in the downstream development of the turbulence intensity in cases S6 and H6 shown in Fig. 20, in the higher TSR cases reported in Gharaati *et al.* [47] the turbulence statistics in the far-wake region appear to be qualitatively similar, with quantitative differences (e.g., the peak magnitude and location) caused by the vertical tilting of the wake.
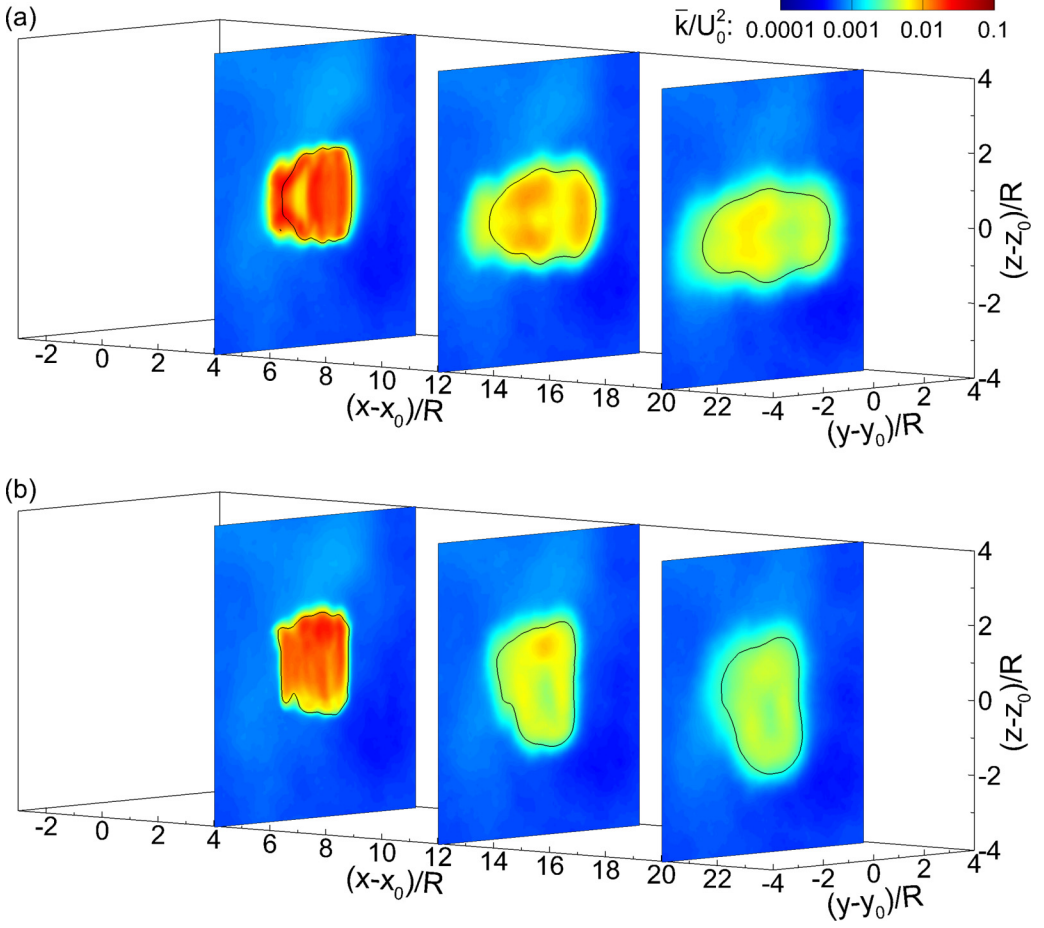
FIG. 20. Time-averaged TKE $\bar{k}$ in flows past VAWTs rotating at $\lambda = 0.6$: (a) straight-bladed VAWT (case S6); (b) helical-bladed VAWT (case H6). The contours of $\bar{k}/U_0^2$ are shown on three representative (y, z) planes at $x - x_0 = 4R$, $12R$ and $20R$. On each plane, the solid isoline of $\bar{u}/U_0 = 0.98$ is used to highlight the edge of the wake region.

D. Torque and power

In this subsection, the performances of the straight- and helical-bladed VAWTs in power generation are quantified and compared. For each turbine blade element, only the wind-induced force projected to the s direction (i.e., the chord direction; see Fig. 24 in Appendix A) contributes to the torque for rotating the VAWT and generating power. Assume the nth element of the mth blade is located at the rotation azimuth angle θ_n^m. The corresponding streamwise and spanwise wind-induced forces are denoted as $F_{n,1}(\theta_n^m)$ and $F_{n,2}(\theta_n^m)$ and calculated based on Eqs. (A1) and (A2), respectively (see Appendix A). Projecting $F_{n,1}$ and $F_{n,2}$ to the s direction yields

$$F_{n,s}(\theta_n^m) = F_{n,1}(\theta_n^m) \sin \theta_n^m - F_{n,2}(\theta_n^m) \cos \theta_n^m. \tag{4}$$

The instantaneous wind-induced torque on the VAWT can be calculated as

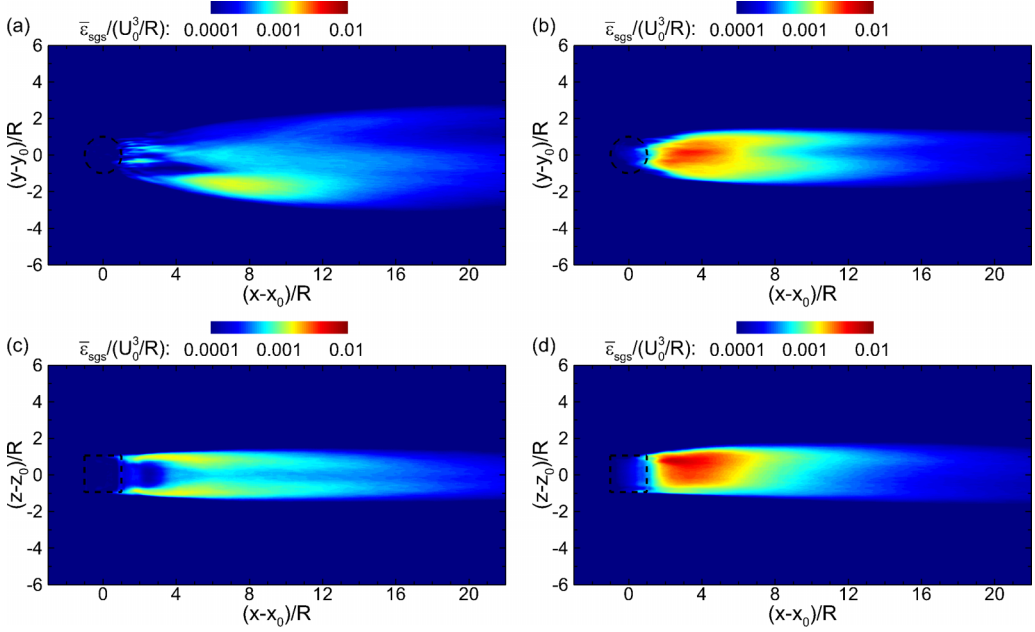$$\tau = \sum_{m=1}^{N_b} \sum_{n=1}^{N_e} F_{n,s}(\theta_n^m) R, \tag{5}$$

FIG. 21. Time-averaged subgrid-scale turbulence dissipation rate $\overline{\varepsilon}_{sgs} = \overline{\nu_\tau \frac{\partial \tilde{u}_i}{\partial x_j} \frac{\partial \tilde{u}_i}{\partial x_j}}$ in flows past VAWTs rotating at $\lambda = 0.6$: (a), (c) straight-bladed VAWT (case S6); (b), (d) helical-bladed VAWT (case H6). The top-row panels (a), (b) show the (x, y) plane across the rotor center height (at $z = z_0$), and the bottom-row panels (c), (d) show the (x, z) plane across the rotor axis (at $y = y_0$). In each panel, the VAWT rotor region is denoted by the dashed lines.

and the resulted power generation rate is

$$P = \tau \Omega = \tau \frac{\lambda U_0}{R}. \tag{6}$$

The corresponding torque and the power coefficients are defined as

$$C_\tau = \frac{\tau}{\rho H R^2 U_0^2}, \tag{7}$$

$$C_p = \frac{P}{\rho H R U_0^3}. \tag{8}$$

Figure 22 shows the time evolution of the VAWT torque coefficient C_τ and power coefficient C_p within one full rotation period T_0 for all four cases S6, S4, H6, and H4. The straight-bladed VAWT cases exhibit five distinct peaks in the C_τ and C_p curves, corresponding to the five straight blades when each rotates to the favorable azimuth angle range for torque generation (i.e., when θ is within the range of about $220°$–$320°$). Two representative instant times $t = 7.68$ s and 7.70 s are chosen based on the torque curve of case S6 shown in Fig. 22. The corresponding instantaneous flow fields are shown in Fig. 23, and the torque contributions from different VAWT blades are listed in Table III.

In cases S6 and S4, the straight-bladed VAWT experienced five short periods of negative instantaneous torque and power during the rotation as shown in Fig. 22. This phenomenon, the "Dead Zone" [96], is a known issue when straight-bladed VAWTs rotate at low TSRs [96–99]. In cases S6 and S4, the VAWT was able to escape the dead zone with the angular momentum of the rotation gained from the periods of positive torque. But the instantaneous torque and power of the VAWT exhibit noticeable temporal variations as shown in Fig. 22 (see the solid and dash-dot lines).
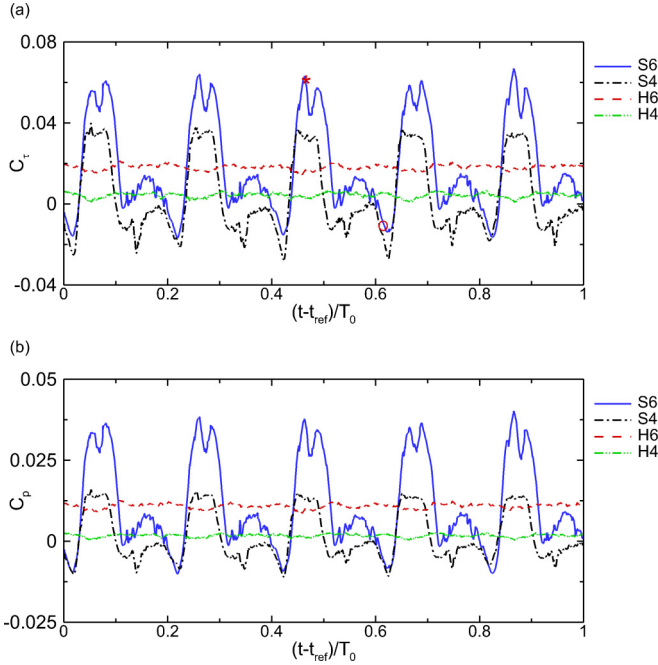
FIG. 22. Time series of VAWT (a) torque coefficient C_τ and (b) power coefficient C_p within one rotation period T_0 (starting from $t_{ref} = 7.60$ s) for different cases: ——, S6; $-\cdot-$, S4; $--$, H6; $-\cdot\cdot-$, H4. For the two instant times of case S6 marked in panel (a), $*$ for $t = 7.68$ s and $\circ$ for $t = 7.70$ s, the corresponding (x, y) plane views of the instantaneous flow field are shown in Fig. 23.

In contrast, the twisted blades of the helical VAWT allow different vertical sections of the blades to cover the full range of θ continuously during the rotation, resulting in much smoother time evolution of C_τ and C_p (see the dashed and dash-dot-dot curves in Fig. 22). Table IV summarizes the mean values and RMS deviations of C_p for the four simulation cases. At the higher TSR of $\lambda = 0.6$, both the straight-bladed and helical-bladed VAWTs (cases S6 and H6) show comparable mean power coefficient at around 0.02, but the RMS deviation of C_p in case H6 is one order of magnitude smaller than that in case S6. At the lower TSR of $\lambda = 0.4$, both VAWTs show low mean values for
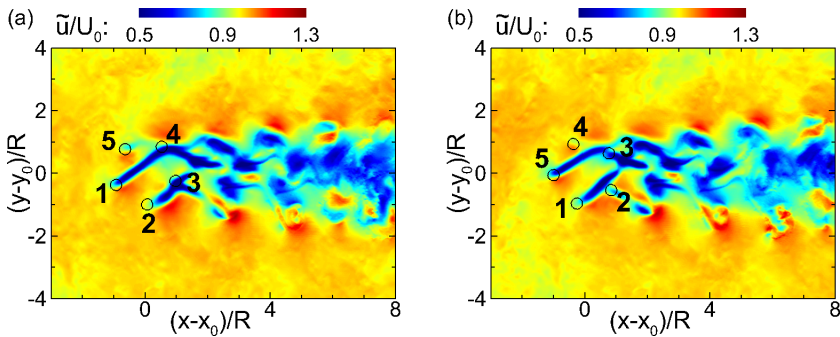

FIG. 23. Instantaneous streamwise velocity on the (x, y) plane at $z = z_0$ for case S6 at the two instant times marked in Fig. 22(a): (a) at $t = 7.68$ s; (b) at $t = 7.70$ s. The five blades of the straight VAWT are labeled, and the corresponding instantaneous torque coefficients of different blades are listed in Table III.

TABLE III. Torque contribution from every blade in case S6 at the two instant times shown in Fig. 23.

	t = 7.68 s		t = 7.70 s	
Blades	θ	C_τ	θ	C_τ
1	21	−0.008	75	−0.006
2	93	0.0006	147	−0.0013
3	165	0.0014	219	0.0035
4	237	0.029	291	0.0115
5	309	0.038	3	−0.0177

the C_p, indicating that the VAWTs are not operating at an optimal condition at this low TSR. It should be noted that $\lambda = 0.6$ is chosen based on the rotating speed of the helical-bladed VAWT observed in the wind tunnel test (see Sec. III). The simulation cases for $\lambda = 0.4$ were performed to illustrate that the key effects of the blade geometry on the VAWT wake characteristics observed at $\lambda = 0.6$ still persist at other lower TSRs. Note that the temporal variations of the power generation rate by wind turbines usually are managed using some power control mechanisms [10,11,13]. The relatively low temporal fluctuations of C_p shown in cases H6 and H4 suggest that using helical-shaped blades may help simplify the power control module of the VAWT, which may lead to less frequent maintenance and lower maintenance cost. The lower temporal fluctuations achieved by the helical blades may also help reduce the fatigue loads to extend the lifespan of the turbine [100].

It should be pointed out that the VAWTs considered in this study were not optimized for high power efficiency at low TSR. The relatively low mean power coefficients shown in Table III were needed to balance the friction effect of the center shaft for the VAWTs to rotate steadily in the wind tunnel test (see Sec. III). It is a commonly recognized challenge for VAWTs to maintain high power coefficient at low TSRs due to the effect of dynamic stalls [101]. It remains an active research area to optimize the VAWT performance at low TSRs [98,102], which goes beyond the scope of the current study. Note that for the commercial helical-bladed VAWT studied in Wei *et al.* [29] and Gharaati *et al.* [47], the measured power coefficients were in the range of 0.04–0.09 at $\lambda = 1.19$–1.40. The mean power coefficients for cases S6 and H6 considered in this study are lower but still have the same order of magnitude, suggesting that they may be adequate to serve as supplementary power sources for urban applications.

V. CONCLUSIONS AND DISCUSSION

In this study, the turbulent flows past straight- and helical-bladed VAWTs rotating at relatively low tip speed ratios are simulated using LES and ALM. Both the straight- and helical-bladed VAWTs have identical key parameters, including the rotor radius and height, blade number, blade cross-sectional geometry. The flows past these two VAWTs were simulated at two TSRs, $\lambda = 0.6$ (chosen based on the wind tunnel test) and $\lambda = 0.4$ (chosen to be arbitrarily low for comparison

TABLE IV. Mean values and RMS deviations of the power coefficient C_p.

Case	C_p mean	C_p RMS deviation
S6	1.07×10^{-2}	1.37×10^{-2}
S4	1.15×10^{-3}	7.97×10^{-3}
H6	1.06×10^{-2}	8.78×10^{-4}
H4	1.60×10^{-3}	5.24×10^{-4}

purposes). The simulation results are analyzed and compared to help elucidate the effects of the blade geometry on the wake flow characteristics.

Direct observation of the instantaneous flow fields shows that the wake behind the straight-bladed VAWT experiences transition from quasilaminar 2D flow motions in the (x, y) plane in the near-wake region to 3D turbulence in the far-wake region. Consequently, the mean wake flow exhibits growth mainly in the spanwise direction as the wake extends downstream. In contrast, the wake flow behind helical-bladed VAWT exhibits considerable 3D features even in the near-wake region. The combination of the blade twist and rotating direction of the helical-bladed VAWT generates a screwdriver effect, resulting in a mean wake flow pattern of upward flows at around $y - y_0 = \pm R$ accompanied by downward flows adjacent to them on the inner side of the wake region. This mean vertical flow pattern causes the wake behind the helical-bladed VAWT to grow mainly in the vertical direction, with negligible growth of the spanwise width as the wake extends downstream.

Furthermore, statistical analyses of the velocity fluctuations show that the wake of the straight-bladed VAWT has weaker SGS turbulence dissipation than that of the helical-bladed VAWT. Consequently, the helical-bladed VAWT helps reduce the turbulence intensity of the wake flow in the far-wake region. Combining the smaller spanwise width and the lower turbulence intensity of the far-wake region, the simulation results obtained from the current LES study suggest that potential impacts (e.g., reduced wind speed, increased velocity fluctuation) of the upstream VAWTs on other VAWTs located downstream can be less significant in the helical-bladed VAWT case. Thus, it may be beneficial to employ the helical-bladed design instead of the straight-bladed design if multiple VAWTs need to be deployed in an array configuration for power extraction. Note that these benefits do not come with the price of reduced power extraction, since the helical-bladed VAWT showed comparable mean value and lower RMS deviation of the power coefficient when compared with the straight-bladed VAWT.

It should be noted that this study focuses on investigating the effects of helical blades on the VAWT wake characteristics. The straight- and helical-bladed VAWTs modeled in LES are based on a specific set of key parameters (see Table I), and only one blade twist angle is considered due to the high computational cost of each simulation case. As pointed out in Sec. IV, although some qualitative comparison may be made between the current LES cases and the higher TSR cases reported in Gharaati *et al.* [47], a more quantitative comparison cannot be made directly because the VAWT parameters and the inflow conditions considered in the two studies are very different. Nevertheless, the differences in the wake flow characteristics between the straight- and helical-bladed VAWTs reported in the current study appear to be limited to low TSR conditions. Araya *et al.* [23] proposed to use the dynamic solidity defined as $\sigma_D = 1 - 1/2\pi\sigma\lambda$ to characterize the wake flows of different VAWTs, and showed that increasing σ_D leads to an earlier transition of the VAWT wake to bluff-body dynamics similar to the flow past a cylinder. For the S6 and H6 cases considered in this study, the corresponding value is $\sigma_D \approx -0.15 < 0$, indicating that VAWT wake behaves less like that past a cylinder in both near- and far-wake regions [23]. Indeed, as shown by the instantaneous and time-averaged flows in Sec. IV, the wake flows exhibit more of the collective effects of individual wakes from each blade at the low TSRs. For comparison, the cases studied in Gharaati *et al.* [47] and Wei *et al.* [29] have $\sigma_D \approx 0.51$. As a result, the overall characteristics of the far-wake for the straight- and helical-bladed VAWTs appear to be qualitatively similar; the helical blades induce additional mean vertical motion in the near-wake region to affect the mean velocity and turbulence statistics.
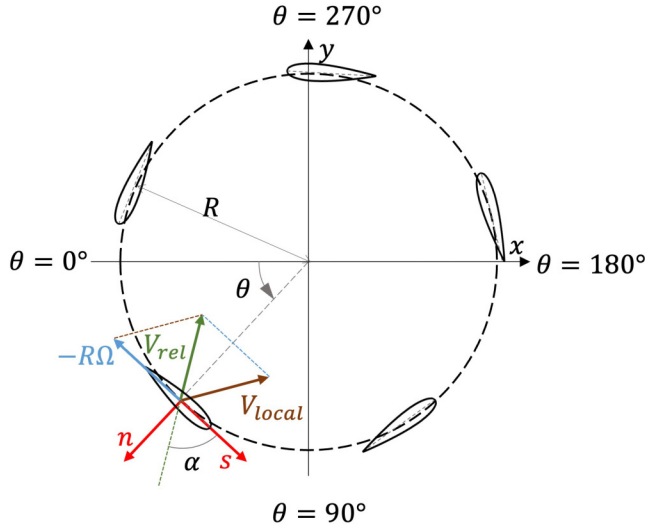
FIG. 24. Schematics of the physical quantities involved in the modeling of the VAWT blade forces.

APPENDIX A: ACTUATOR LINE METHOD FOR MODELING WIND TURBINE

In the current LES modeling framework, the effect of the rotating VAWT blades on the flow is modeled using the ALM. Assume the VAWT rotor has a radius of R (the radial distance from the chord of each blade to the center axis of the VAWT). It consists of N_b blades. Each blade has a chord length of c, a cross-sectional thickness of t_b, and a vertical height of H. The rotor rotates at the angular speed of Ω counterclockwise.

In the LES model, each VAWT blade is discretized evenly into N_e elements, with a vertical height of $\Delta H = H/N_e$ for each element. For the nth element of a VAWT blade, the aerodynamic force acting on it is $\mathbf{F}_n = F_{n,1}\hat{\mathbf{e}}_1 + F_{n,2}\hat{\mathbf{e}}_2$, where $\hat{\mathbf{e}}_1$ and $\hat{\mathbf{e}}_2$ are the unit vectors in the x and y directions, respectively. The force components are computed as

$$F_{n,1} = -\tfrac{1}{2}\rho V_{\mathrm{rel}}^2 c\,\Delta H[C_L^* \cos(\theta + \alpha) + C_D^* \sin(\theta + \alpha)], \tag{A1}$$

$$F_{n,2} = \tfrac{1}{2}\rho V_{\mathrm{rel}}^2 c\,\Delta H[-C_L^* \sin(\theta + \alpha) + C_D^* \cos(\theta + \alpha)]. \tag{A2}$$

As illustrated in Fig. 24, $\mathbf{V}_{\mathrm{rel}}$ is the relative horizontal velocity vector of the local air inflow with respect to the blade element, where

$$\mathbf{V}_{\mathrm{rel}} = (\widetilde{u} - R\,\Omega \sin\theta)\hat{\mathbf{e}}_1 + (\widetilde{v} + R\,\Omega \cos\theta)\hat{\mathbf{e}}_2; \tag{A3}$$

V_{rel} is the magnitude of $\mathbf{V}_{\mathrm{rel}}$; θ is the azimuth angle of the blade rotation; C_L^* and C_D^* are the lift and drag coefficients with dynamic stall correction [103]; and α is the local angle of attack of the inflow

relative to the rotating blade calculated based on

$$\alpha = \arctan\left(\frac{-\cos(\theta - \beta)}{-\sin(\theta - \beta) + R\,\Omega/\widetilde{U}_h}\right), \tag{A4}$$

where $\beta = \arctan(\widetilde{v}/\widetilde{u})$ is the horizontal directional angle of the inflow wind velocity, and $\widetilde{U}_h = \sqrt{\widetilde{u}^2 + \widetilde{v}^2}$ is the magnitude of the inflow horizontal velocity.

In the present study, the modified Boeing-Vertol model [104] is used to model the effect of dynamic stall [103] caused by the rapid changes in angle of attack when the VAWT blades rotate in turbulent flow. In particular, the effective angles of attack to be used for determining the lift and drag coefficients are modeled as [104]

$$\alpha_L^* = \alpha - \gamma_L \kappa \sqrt{\left|\frac{c\dot{\alpha}}{2V_{\text{rel}}}\right|}\,\frac{\dot{\alpha}}{|\dot{\alpha}|}, \tag{A5}$$

$$\alpha_D^* = \alpha - \gamma_D \kappa \sqrt{\left|\frac{c\dot{\alpha}}{2V_{\text{rel}}}\right|}\,\frac{\dot{\alpha}}{|\dot{\alpha}|}, \tag{A6}$$

respectively, where $\dot{\alpha} = d\alpha/dt$ is the instantaneous rate of change of α, and γ_L, γ_D and κ are dimensionless model coefficients expressed as

$$\gamma_L = 1.4 - 6\left(0.06 - \frac{t_b}{c}\right), \tag{A7}$$

$$\gamma_D = 1 - 2.5\left(0.06 - \frac{t_b}{c}\right), \tag{A8}$$

$$\kappa = 0.75 + 0.25\frac{\dot{\alpha}}{|\dot{\alpha}|}. \tag{A9}$$

Based on α_L^* and α_D^*, the lift and drag coefficients with the dynamic stall correction are computed as [104]

$$C_L^* = \left(\frac{\alpha}{\alpha_L^* - \alpha_0}\right)C_L(\alpha_L^*), \tag{A10}$$

$$C_D^* = C_D(\alpha_D^*), \tag{A11}$$

where α_0 is the angle of zero lift, which is equal to 0 for symmetric airfoils, and C_L and C_D are the static lift and drag coefficients for the airfoil shape of the VAWT blade cross section, respectively. The values of C_L^* and C_D^* obtained from Eqs. (A10) and (A11) are used in Eqs. (A1) and (A2) to obtain the two components of the total aerodynamic force for the nth blade element.

Applying $\mathbf{F}_n$ as a local point force in the LES model may lead to numerical instability. To avoid numerical instability and reduce sensitivity of the model to the grid resolution, the blade-induced aerodynamic force is usually distributed smoothly over a number of grid points in the vicinity of the blade element [24,40,57,105]. In the current LES model, the widely used three-dimensional Gaussian kernel method [57–60] is employed to smoothly distribute the aerodynamic force in the discretized computational domain. The distributed body forces $f_{\epsilon,i}(i = 1, 2)$ used in Eq. (2) are calculated based on

$$f_{\epsilon,i}(x, y, z) = \sum_{n=1}^{N_e} F_{n,i}G_n(x, y, z), \tag{A12}$$

where $F_{n,i}(i = 1, 2)$ are given by Eqs. (A1) and (A2),

$$G_n(x, y, z) = \epsilon^{-3}\pi^{-3/2}\exp\left(-r_n^2/\epsilon^2\right) \tag{A13}$$

is the Gaussian kernel function, $r_n = \sqrt{(x - x_n)^2 + (y - y_n)^2 + (z - z_n)^2}$ is the distance between a space point (x, y, z) and the center point of the nth blade element (x_n, y_n, z_n), and ϵ is the kernel

width. The specific value of ϵ used in the present LES study is given in Sec. III. Moreover, an accumulative function based on the superposition of blade-element Gaussian kernel is constructed as

$$G_b(x, y, z) = \sum_{n=1}^{N_e} G_n(x, y, z) \Delta x \Delta y \Delta z. \tag{A14}$$

In this paper, the isosurfaces of G_b are used to visualize the turbine blade locations and the overall VAWT geometry (straight or helical).

APPENDIX B: INFLOW BOUNDARY CONDITION BASED ON JHTDB

The LESGO model uses the Fourier-series-based pseudospectral method for the spatial discretizations in the x direction. By default it assumes that the simulated flow is periodic in the x direction. This is not compatible with the inflow–outflow conditions required for simulating wind turbine wake flows. To overcome this issue, a fringe-zone method [106] has been implemented in LESGO and has been successfully used in various LES studies of nonperiodic flows [47,65,107]. In particular, a fringe zone of finite streamwise length L_{fr} adjacent to the outflow boundary (at $x = L_x$) is used to force the simulated flow velocity in the far wake of VAWT to smoothly transition back to the imposed value at the inflow boundary (at $x = 0$). Within the fringe zone, the flow velocity vector is imposed as

$$\widetilde{u}_i(x, y, z, t) = \widetilde{u}_i(x_{fr}, y, z, t)[1 - \psi(x)] + u_{\mathrm{in},i}(y, z, t)\psi(x), \quad \text{at } x \in [x_{fr}, L_x], \tag{B1}$$

where L_x is the streamwise length of the simulation domain, $x_{fr} = L_x - L_{fr}$ is the streamwise location where the fringe zone starts, $\psi(x) = 0.5 - 0.5\cos[\pi(x - x_{fr})/L_{fr}]$ is the fringe function, and $u_{\mathrm{in},i}(i = 1, 2, 3) = (u_{\mathrm{in}}, v_{\mathrm{in}}, w_{\mathrm{in}})$ is the imposed instantaneous velocity vector at the LES inflow boundary.

Following Martínez-Tossas *et al.* [63], in this study we use the simulation data of HIT from JHTDB [62] to construct the turbulent inflow condition for the LES. In particular, the inflow velocity consists of a uniform mean velocity U_0 and a fluctuating velocity field from JHTDB. In turbulent flows, the turbulence intensity is defined as $I_t \equiv \sqrt{2k/3}/U_0$, where $k = 0.5[(u'_{\mathrm{RMS}})^2 + (v'_{\mathrm{RMS}})^2 + (w'_{\mathrm{RMS}})^2]$ is turbulent kinetic energy with $(u'_{\mathrm{RMS}}, v'_{\mathrm{RMS}}, w'_{\mathrm{RMS}})$ being the root-mean-square (RMS) values for the fluctuations of the three velocity components. In the HIT, $u'_{\mathrm{RMS}} = v'_{\mathrm{RMS}} = w'_{\mathrm{RMS}}$ and the turbulence intensity becomes $I_t = u'_{\mathrm{RMS}}/U_0$. The HIT data in JHTDB were obtained from a direct numerical simulation (DNS) in a 1024^3 periodic box at a Taylor-scale Reynolds number of $\mathrm{Re}_\lambda = u'_{\mathrm{RMS}}\lambda/\nu \approx 433$, where λ is the Taylor microscale. The DNS database velocities are transformed to the velocities suitable for LES inflow condition based on the following conditions [63]:

$$I_t = \frac{u'_{\mathrm{RMS}}}{U_0} = \frac{u'_{\mathrm{RMS}}|_{\mathrm{DB}}}{U_0|_{\mathrm{DB}}}, \tag{B2}$$

where u'_{RMS} is the desired RMS velocity of the LES, U_0 is the desired mean inflow velocity of the LES, $u'_{\mathrm{RMS}}|_{\mathrm{DB}}$ is the RMS velocity of the database, and $U_0|_{\mathrm{DB}}$ is a sweep velocity for properly extracting the HIT data from the database (since there is no mean velocity in the original DNS of the HIT). Matching the desired turbulence intensity yields

$$U_0|_{\mathrm{DB}} = \frac{u'_{\mathrm{RMS}}|_{\mathrm{DB}}}{I_t}. \tag{B3}$$

Based on $U_0|_{\mathrm{DB}}$, a time-evolving turbulence velocity field is extracted from the HIT database, which is transformed to LES inflow velocities $u_{\mathrm{in},i}(y, z, t)$ according to [63]

$$u_{\mathrm{in}}(y, z, t) = U_0 + u_{\mathrm{DB}}(x_{\mathrm{DB}}, y_{\mathrm{DB}}, z_{\mathrm{DB}}, t_{\mathrm{DB}}) \frac{U_0}{U_0|_{\mathrm{DB}}}, \tag{B4}$$

$$v_{\text{in}}(y, z, t) = v_{\text{DB}}(x_{\text{DB}}, y_{\text{DB}}, z_{\text{DB}}, t_{\text{DB}}) \frac{U_0}{U_0|_{\text{DB}}}, \tag{B5}$$

$$w_{\text{in}}(y, z, t) = w_{\text{DB}}(x_{\text{DB}}, y_{\text{DB}}, z_{\text{DB}}, t_{\text{DB}}) \frac{U_0|_{\text{LES}}}{U_0|_{\text{DB}}}. \tag{B6}$$

Here y, z, and t are the spanwise and vertical coordinates and time used in the LES, respectively; $(x_{\text{DB}}, y_{\text{DB}}, z_{\text{DB}})$ are the corresponding space coordinates in the database; t_{DB} is the corresponding flow time in the database; and $(u_{\text{DB}}, v_{\text{DB}}, w_{\text{DB}})$ is the instantaneous velocity vector extracted from the database, which is the same as the turbulent velocity fluctuation $(u'_{\text{DB}}, v'_{\text{DB}}, w'_{\text{DB}})$ since there is no mean flow in the HIT. Let L_y be the spanwise length of the LES domain and $L_y|_{\text{DB}}$ be the spanwise length of the DNS domain for the database, the desired values of space coordinates and time for data extraction are calculated based on [63]

$$x_{\text{DB}} = -U_0|_{\text{DB}} \, t_{\text{DB}}, \tag{B7}$$

$$y_{\text{DB}} = y \, \frac{L_y|_{\text{DB}}}{L_y}, \tag{B8}$$

$$z_{\text{DB}} = z \, \frac{L_y|_{\text{DB}}}{L_y}, \tag{B9}$$

$$t_{\text{DB}} = t \, \frac{L_y|_{\text{DB}}}{L_y} \, \frac{U_0}{U_0|_{\text{DB}}}. \tag{B10}$$

The inflow velocity components obtained based on Eqs. (B4)–(B6) are used in the fringe-zone method (B1) to provide the turbulent inflow condition for the LES. This inflow prescription method of using the JHTDB HIT data has been successfully applied by Gharaati *et al.* [47] in a test case for validating the current LES-ALM model of VAWT wake flows. In that validation case, the LES model was used to reproduce the towing-tank experiment of flow past a straight-bladed VAWT [15], and showed good agreement with the experimental data [47]. In the present study, the same inflow prescription method is used to study the effects of blade geometry on the VAWT wake flow characteristics.

APPENDIX C: GRID RESOLUTION TEST

In the reported LES cases, 281 grid points were used to discretize the vertical domain height $L_z = 2.0$ m, resulting in a grid resolution of $\Delta z = 0.0071$ m. Within the VAWT rotor height H, this vertical grid resolution provides about 42 grid points to capture the flow physics. On the (x, y) plane, the horizontal grid resolutions used in the LES need to be able to model the effect of the blade-induced aerodynamic force on the air flow. In the current LES model, the ALM is used to model the turbine blade effect, which requires a specification of the Gaussian kernel size ϵ. Previous potential flow theory analysis of flow past airfoil performed by Martínez-Tossas *et al.* [85] suggested that the value of ϵ should be chosen to be close to $\epsilon/c \sim O(0.4)$. To model the VAWTs considered in this study which have $c = 0.043$ m, we set $\epsilon = 0.02$ cm. This yields a ratio of $\epsilon/c = 0.47$.

Previous LES ALM modeling studies of wind turbine flows [e.g., 57,58,84] also suggested that the ratio of the Gaussian kernel size to the horizontal grid size should satisfy $\epsilon/\Delta x > 2$ (note that $\Delta x = \Delta y$ in the current LES) in order to avoid numerical instability caused by applying localized force in the LES flow solver. Based on $\epsilon = 0.02$ m and the stability requirement of $\epsilon/\Delta x > 2$, three different grid resolutions were tested for case H4 in order to confirm the choice of grid numbers used in the current LES. The grid numbers and the corresponding grid resolutions of these three cases are summarized in Table V. In particular, case H4 used the same number of grid points of $N_x \times N_y \times N_z = 864 \times 384 \times 281$ as other cases listed in Table II. Case H4-HR used more horizontal grid points ($N_x \times N_y \times N_z = 1152 \times 512 \times 373$) and case H4-LR used fewer horizontal grid points ($N_x \times N_y \times N_z = 576 \times 256 \times 187$) than case H4. For all three cases, a fixed simulation time step of

TABLE V. LES parameters for grid resolution tests based on case H4.

Case	Grid number $N_x \times N_y \times N_z$	Grid resolution $(\Delta x, \Delta y, \Delta z)$	Gaussian kernel size ϵ	$\epsilon/\Delta x$
H4-HR	$1152 \times 512 \times 373$	$(0.0039, 0.0039, 0.0054)\,\mathrm{m}$	$0.02\,\mathrm{m}$	5.1
H4	$864 \times 384 \times 281$	$(0.0052, 0.0052, 0.0071)\,\mathrm{m}$	$0.02\,\mathrm{m}$	3.8
H4-LR	$576 \times 256 \times 187$	$(0.0078, 0.0078, 0.0107)\,\mathrm{m}$	$0.02\,\mathrm{m}$	2.6

$\Delta t = 2.0 \times 10^{-5}$ s was used in the LES. Note that case H4 was chosen for the grid resolution test because it has the same level of grid resolution requirement as case H6, but the VAWT rotates at a lower TSR of $\lambda = 0.4$ that relaxes the stability requirement on the simulation time step. Choosing $\lambda = 0.4$ allows us to complete the high-resolution test case H4-HR with reasonable computational cost.

Figure 25 compares the (x, y) and (x, z) planar views of the time-averaged streamwise velocity $\bar{u}$ obtained from three grid-resolution test cases, and Fig. 26 shows the corresponding spanwise
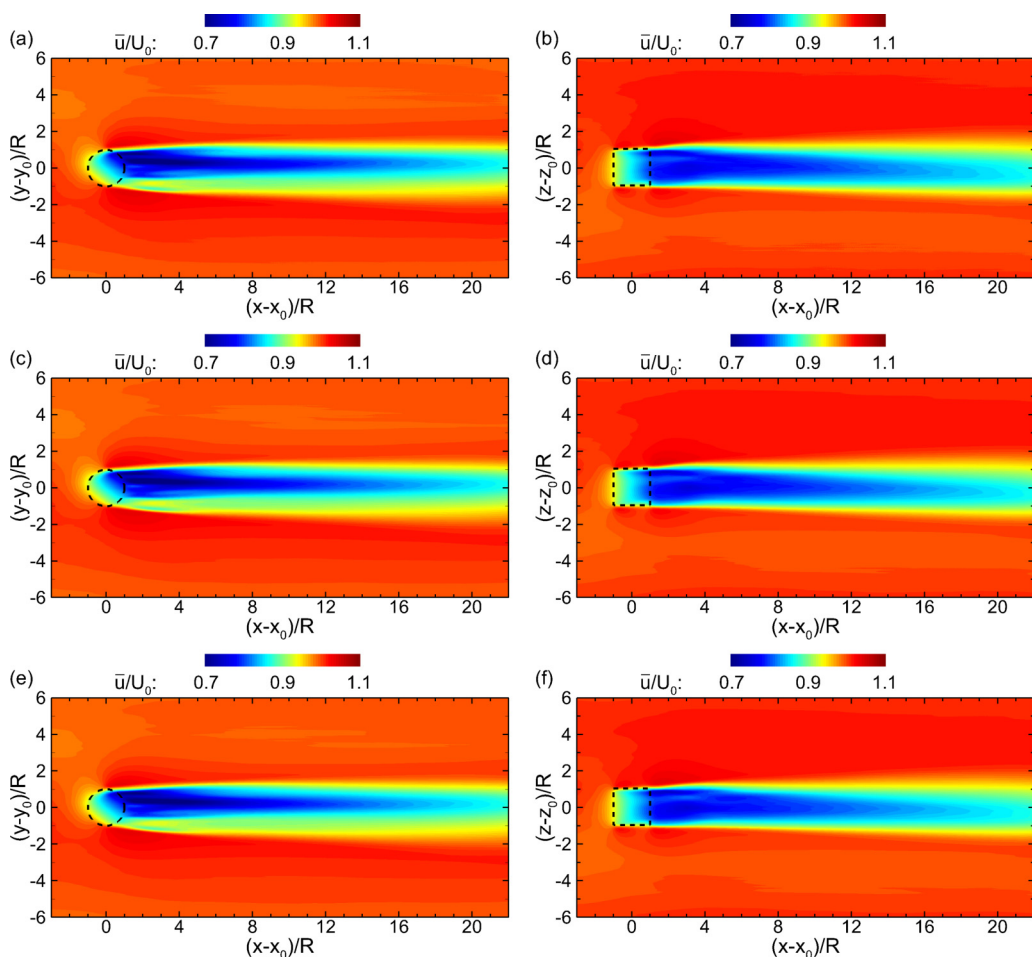

FIG. 25. Time-averaged streamwise velocity $\bar{u}$ in flow past helical-bladed VAWT rotating at $\lambda = 0.4$. The results were obtained from LES test runs with different grid point numbers, $N_x \times N_y \times N_z =$: (a), (b) $1152 \times 512 \times 373$ (case H4-HR); (c), (d) $864 \times 384 \times 281$ (case H4); (e), (f) $576 \times 256 \times 187$ (case H4-LR).
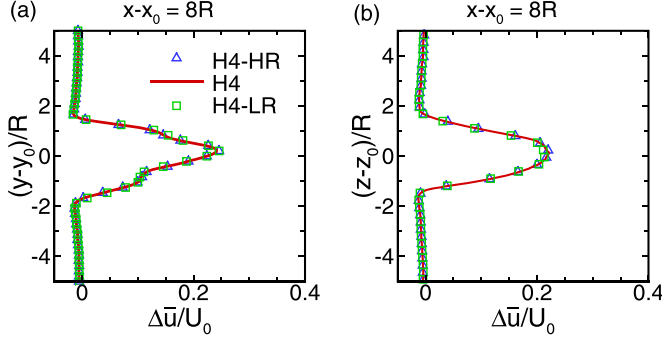
FIG. 26. Spanwise (a) and vertical (b) profiles of mean streamwise velocity deficit $\Delta\bar{u}$ at $x - x_0 = 8R$ downstream of the helical-bladed VAWT rotating at $\lambda = 0.4$: $\triangle$, case H4-HR; ——, case H4; $\square$, case H4-LR. The symbols are plotted for every four vertical grid points for case H4-LR and every eight vertical grid points for case H4-HR, respectively.

and vertical profiles of $\Delta\bar{u}$ at $x - x_0 = 8R$. The results obtained from the three test cases are very similar, suggesting that grid resolutions used in the current LES study are sufficient. For all other simulation cases, we used the intermediate grid numbers of $N_x \times N_y \times N_z = 864 \times 384 \times 281$, as listed in Table II.

APPENDIX D: TIME AVERAGE STATISTICS CONVERGENCE TEST

To confirm the convergence of the turbulence statistics, we tested the time average using 8304 and 4152 instantaneous snapshots of the flow field. Here the straight-bladed VAWT rotating at $\lambda = 0.6$ is used for demonstration. In particular, the time-average analysis based on 8304 samples is referred to as case S6 (the same case reported in Sec. IV B), and the time-average analysis based on 4152 samples is referred to as case S6-S (the same configuration as case S6 but with 50% shorter duration and less samples).

Figures 27 and 28 compare the vertical profiles of mean velocity deficit $\Delta\bar{u}$, mean kinetic energy $\bar{k}$ and Reynolds shear stress component $\overline{u'w'}$ at $x - x_0 = 4R$ and $8R$, respectively. Figures 29 and 30 compare the spanwise profiles of mean velocity deficit $\Delta\bar{u}$, mean kinetic energy $\bar{k}$ and Reynolds shear stress component $\overline{u'v'}$ at $x - x_0 = 4R$ and $8R$, respectively. As shown in these figures, the
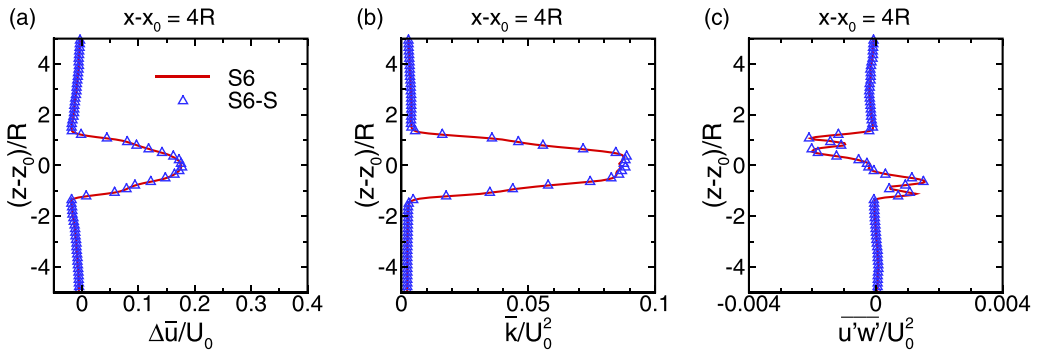

FIG. 27. Vertical profiles of (a) mean velocity deficit $\Delta\bar{u}$, (b) mean kinetic energy $\bar{k}$, and Reynolds shear stress component $\overline{u'w'}$ at $x - x_0 = 4R$ downstream of the straight-bladed VAWT rotating at $\lambda = 0.6$: ——, case S6; $\triangle$, case S6-S (which uses 50% fewer samples for time average than case S6). The symbols are plotted for every three grid points used in LES.

FIG. 28. Vertical profiles of (a) mean velocity deficit $\Delta \overline{u}$, (b) mean kinetic energy $\overline{k}$, and Reynolds shear stress component $\overline{u'w'}$ at $x - x_0 = 8R$ downstream of the straight-bladed VAWT rotating at $\lambda = 0.6$: ——, case S6; $\triangle$, case S6-S (which uses 50% fewer samples for time average than case S6). The symbols are plotted for every three grid points used in LES.
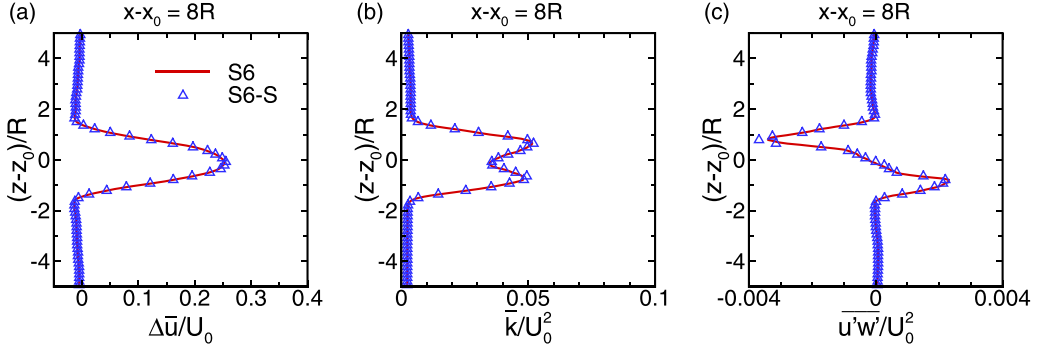

FIG. 29. Spanwise profiles of (a) mean velocity deficit $\Delta \overline{u}$, (b) mean kinetic energy $\overline{k}$, and Reynolds shear stress component $\overline{u'v'}$ at $x - x_0 = 4R$ downstream of the straight-bladed VAWT rotating at $\lambda = 0.6$: ——, case S6; $\triangle$, case S6-S (which uses 50% fewer samples for time average than case S6). The symbols are plotted for every four grid points used in LES.

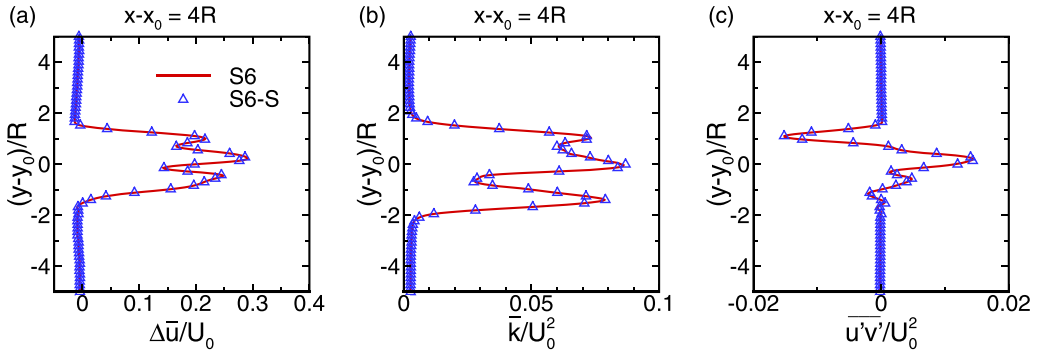FIG. 30. Spanwise profiles of (a) mean velocity deficit $\Delta \overline{u}$, (b) mean kinetic energy $\overline{k}$, and Reynolds shear stress component $\overline{u'v'}$ at $x - x_0 = 8R$ downstream of the straight-bladed VAWT rotating at $\lambda = 0.6$: ——, case S6; $\triangle$, case S6-S (which uses 50% fewer samples for time average than case S6). The symbols are plotted for every four grid points used in LES.
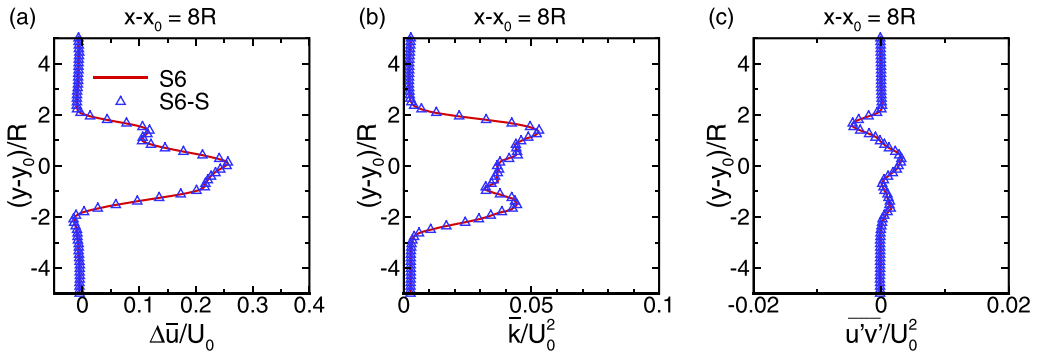
statistics obtained using 8304 (case S6) and 4152 samples (case S6-S) agree well, confirming that the time-average statistics have converged. For all the cases shown in Sec. IV, the statistical results based on 8304 samples are presented.

[1] S. Potrč, L. Čuček, M. Martin, and Z. Kravanja, Sustainable renewable energy supply networks optimization—The gradual transition to a renewable energy system within the European Union by 2050, Renewable Sustainable Energy Rev. **146**, 111186 (2021).

[2] J. Lee and F. Zhao, Global Wind Report 2022, Tech. Rep. (Global Wind Energy Council, 2022).

[3] J. F. Manwell, J. G. McGowan, and A. L. Rogers, *Wind Energy Explained: Theory, Design and Application*, 2nd ed. (Wiley, Chichester, England, UK, 2009).

[4] T. Burton, N. Jenkins, D. Sharpe, and E. Bossanyi, *Wind Energy Handbook* (Wiley, Chichester, England, UK, 2011).

[5] F. Porté-Agel, M. Bastankhah, and S. Shamsoddin, Wind-turbine and wind-farm flows: A review, Boundary-Layer Meteorology **174**, 1 (2020).

[6] J. Contrell, T. Stehly, J. Johnson, J. O. Roberts, Z. Parker, G. Scott, and D. Heimiller, Analysis of transportation and logistics challenges affecting the deployment of larger wind turbines: Summary of results, Tech. Rep. No. NREL/TP-5000-61063 (National Renewable Energy Laboratory, 2014).

[7] M. Kinzel, Q. Mulligan, and J. O. Dabiri, Energy exchange in an array of vertical-axis wind turbines, J. Turbul. **13**, N38 (2012).

[8] G. Brochier, P. Fraunie, C. Beguier, and I. Paraschivoiu, Water channel experiments of dynamic stall on Darrieus wind turbine blades, J. Propul. Power **2**, 445 (1986).

[9] N. Fujisawa and S. Shibuya, Observations of dynamic stall on Darrieus wind turbine blades, J. Wind Eng. Ind. Aerodyn. **89**, 201 (2001).

[10] N. Horiuchi and T. Kawahito, Torque and power limitations of variable speed wind turbines using pitch control and generator power control, in *2001 Power Engineering Society Summer Meeting. Conference Proceedings (Cat. No.01CH37262)* (Vancouver, BC, Canada, 2001), Vol. 1, p. 638.

[11] T. Senjyu, R. Sakamoto, N. Urasaki, T. Funabashi, H. Fujita, and H. Sekine, Output power leveling of wind turbine Generator for all operating regions by pitch angle control, IEEE Trans. Energy Convers. **21**, 467 (2006).

[12] C. Simão Ferreira, G. van Kuik, G. Van Bussel, and F. Scarano, Visualization by PIV of dynamic stall on a vertical axis wind turbine, Exp. Fluids **46**, 97 (2009).

[13] A. S. Yilmaz and Z. Özer, Pitch angle control in wind turbines above the rated wind speed by multi-layer perceptron and radial basis function neural networks, Expert Syst. Appl. **36**, 9767 (2009).

[14] M. M. Aslam Bhutta, N. Hayat, A. U. Farooq, Z. Ali, S. R. Jamil, and Z. Hussain, Vertical axis wind turbine—A review of various configurations and design techniques, Renewable Sustainable Energy Rev. **16**, 1926 (2012).

[15] P. Bachant and M. Wosnik, Performance and near-wake measurements for a vertical axis turbine at moderate Reynolds number, in *Proceedings of the ASME Fluids Engineering Summer Meeting*, FEDSM2013-16575 (ASME, New York City, New York, 2013).

[16] S. Brusca, R. Lanzafame, and M. Messina, Design of a vertical-axis wind turbine: How the aspect ratio affects the turbine's performance, Int. J. Energy Environ. Eng. **5**, 333 (2014).

[17] D. B. Araya and J. O. Dabiri, A comparison of wake measurements in motor-driven and flow-driven turbine experiments, Exp. Fluids **56**, 150 (2015).

[18] M. Kinzel, D. B. Araya, and J. O. Dabiri, Turbulence in vertical axis wind turbine canopies, Phys. Fluids **27**, 115102 (2015).

[19] R. Dunne and B. J. McKeon, Dynamic stall on a pitching and surging airfoil, Exp. Fluids **56**, 157 (2015).

[20] K. J. Ryan, F. Coletti, C. J. Elkins, J. O. Dabiri, and J. K. Eaton, Three-dimensional flow field around and downstream of a subscale model rotating vertical axis wind turbine, Exp. Fluids **57**, 38 (2016).

[21] L. Battisti, A. Brighenti, E. Benini, and M. R. Castelli, Analysis of different blade architectures on small VAWT performance, J. Phys.: Conf. Ser. **753**, 062009 (2016).

[22] D. B. Araya and J. O. Dabiri, Vertical axis wind turbine in a falling soap film, Phys. Fluids **27**, 091108 (2015).

[23] D. B. Araya, T. Colonius, and J. O. Dabiri, Transition to bluff-body dynamics in the wake of vertical-axis wind turbines, J. Fluid Mech. **813**, 346 (2017).

[24] S. H. Hezaveh, E. Bou-Zeid, M. W. Lohry, and L. Martinelli, Simulation and wake analysis of a single vertical axis wind turbine, Wind Energy **20**, 713 (2017).

[25] A. Buchner, J. Soria, D. Honnery, and A. Smits, Dynamic stall in vertical axis wind turbines: Scaling and topological considerations, J. Fluid Mech. **841**, 746 (2018).

[26] S. H. Hezaveh, E. Bou-Zeid, G. Cortina, L. Martinelli, J. Dabiri, and M. Kinzel, Increasing the power production of vertical-axis wind-turbine farms using synergistic clustering, Boundary-Layer Meteorol. **169**, 275 (2018).

[27] I. D. Brownstein, N. J. Wei, and J. O. Dabiri, Aerodynamically interacting vertical-axis wind turbines: Performance enhancement and three-dimensional flow, Energies **12**, 2724 (2019).

[28] S. Shamsoddin and F. Porté-Agel, Effect of aspect ratio on vertical-axis wind turbine wakes, J. Fluid Mech. **889**, R1 (2020).

[29] N. J. Wei, I. D. Brownstein, J. L. Cardona, M. F. Howland, and J. O. Dabiri, Near-wake structure of full-scale vertical-axis wind turbines, J. Fluid Mech. **914**, A17 (2021).

[30] B. LeBlanc and C. Ferreira, Estimation of blade loads for a variable pitch vertical axis wind turbine from particle image velocimetry, Wind Energy **25**, 313 (2022).

[31] C. Pearson, Vertical axis wind turbine acoustics, Ph.D. thesis, Cambridge University, 2013.

[32] K. Dykes, A. Platt, Y. Guo, A. Ning, R. King, T. Parsons, D. Petch, P. Veers, and B. Resor, Effect of tip-speed constraints on the optimized design of a wind turbine, Tech. Rep. No. NREL/TP-5000-61726 (National Renewable Energy Laboratory, 2014).

[33] M. Casini, Small vertical axis wind turbines for energy efficiency of buildings, J. Clean Energy Energy Tech. **4**, 56 (2016).

[34] A. Pourrajabian, M. Dehghan, S. Rahgozar, and D. Wood, Effect of tip speed ratio on the aerodynamic noise of a small wind turbine: An optimization study, J. Phys.: Conf. Ser. **2265**, 042076 (2022).

[35] J. Yen and N. Ahmed, Improving safety and performance of small-scale vertical axis wind turbines, Procedia Eng. **49**, 99 (2012).

[36] C. M. Parker and M. C. Leftwich, The effect of tip speed ratio on a vertical axis wind turbine at high Reynolds numbers, Exp. Fluids **57**, 74 (2016).

[37] J. O. Dabiri, Potential order-of-magnitude enhancement of wind farm power density via counter-rotating vertical-axis wind turbine arrays, J. Renewable Sustainable Energy **3**, 043104 (2011).

[38] S. Shamsoddin and F. Porté-Agel, Large eddy simulation of vertical axis wind turbine wakes, Energies **7**, 890 (2014).

[39] V. Mendoza and A. Goude, Wake flow simulation of a vertical axis wind turbine under the influence of wind shear, J. Phys.: Conf. Ser. **854**, 012031 (2017).

[40] M. Abkar and J. O. Dabiri, Self-similarity and flow characteristics of vertical-axis wind turbine wakes: An LES study, J. Turbul. **18**, 373 (2017).

[41] V. Mendoza, P. Bachant, C. Ferreira, and A. Goude, Near-wake flow simulation of a vertical axis turbine using an actuator line model, Wind Energy **22**, 171 (2019).

[42] V. Mendoza, A. Chaudhari, and A. Goude, Performance and wake comparison of horizontal and vertical axis wind turbines under varying surface roughness conditions, Wind Energy **22**, 458 (2019).

[43] A. Alaimo, A. Esposito, A. Messineo, C. Orlando, and D. Tumino, 3D CFD analysis of a vertical axis wind turbine, Energies **8**, 3013 (2015).

[44] M. Moghimi and H. Motawej, Developed DMST model for performance analysis and parametric evaluation of Gorlov vertical axis wind turbines, Sustainable Energy Technol. Assess. **37**, 100616 (2020).

[45] Q. Cheng, X. Liu, H. S. Ji, K. C. Kim, and B. Yang, Aerodynamic analysis of a helical vertical axis wind turbine, Energies **10**, 575 (2017).

[46] U. Divakaran, A. Ramesh, A. Mohammad, and R. K. Velamati, Effect of helix angle on the performance of helical vertical axis wind turbine, Energies **14**, 393 (2021).

[47] M. Gharaati, S. Xiao, N. J. Wei, L. A. Martínez-Tossas, J. O. Dabiri, and D. Yang, Large-eddy simulation of helical- and straight-bladed vertical-axis wind turbines in boundary layer turbulence, J. Renewable Sustainable Energy **14**, 053301 (2022).

[48] R. H. Kraichnan, Inertial-range transfer in two- and three-dimensional turbulence, J. Fluid Mech. **47**, 525 (1971).

[49] H. Tennekes and J. L. Lumley, *A First Course in Turbulence* (MIT Press, Cambridge, MA, 1996).

[50] G. Boffetta, A. Celani, and M. Vergassola, Inverse energy cascade in two-dimensional turbulence: Deviations from Gaussian behavior, Phys. Rev. E **61**, R29 (2000).

[51] S. Chen, R. E. Ecke, G. L. Eyink, M. Rivera, M. Wan, and Z. Xiao, Inverse energy cascade in two-dimensional turbulence: Deviations from Gaussian behavior, Phys. Rev. Lett. **96**, 084502 (2006).

[52] M. Calaf, C. Meneveau, and J. Meyers, Large eddy simulation study of fully developed wind-turbine array boundary layers, Phys. Fluids **22**, 015110 (2010).

[53] M. Calaf, M. B. Parlange, and C. Meneveau, Large eddy simulation study of scalar transport in fully developed wind-turbine array boundary layers, Phys. Fluids **23**, 126603 (2011).

[54] D. Yang, C. Meneveau, and L. Shen, Large-eddy simulation of offshore wind farm, Phys. Fluids **26**, 025101 (2014).

[55] L. A. Martínez-Tossas, R. J. Stevens, and C. Meneveau, Wind farm large-eddy simulations on very coarse grid resolutions using an actuator line model, AIAA **2016**, 1261 (2016).

[56] S. Shamsoddin and F. Porté-Agel, A large-eddy simulation study of vertical axis wind turbine wakes in the atmospheric boundary layer, Energies **9**, 366 (2016).

[57] J. N. Sørensen and W. Z. Shen, Numerical modeling of wind turbine wakes, J. Fluids Eng. **124**, 393 (2002).

[58] L. A. Martínez-Tossas, M. J. Churchfield, and S. Leonardi, Large eddy simulations of the flow past wind turbines: Actuator line and disk modeling, Wind Energy **18**, 1047 (2015).

[59] L. A. Martínez-Tossas, M. J. Churchfield, and C. Meneveau, A highly resolved large-eddy simulation of a wind turbine using an actuator line model with optimal body force projection, J. Phys.: Conf. Ser. **753**, 082014 (2016).

[60] H. Sarlak, T. Nishino, L. A. Martínez-Tossas, C. Meneveau, and J. N. Sørensen, Assessment of blockage effects on the wake characteristics and power of wind turbines, Renewable Energy **93**, 340 (2016).

[61] M. J. Churchfield, S. Schreck, L. A. Martínez-Tossas, C. Meneveau, and P. R. Spalart, An advanced actuator line method for wind energy applications and beyond, AIAA **2017**, 1998 (2017).

[62] Y. Li, E. Perlman, M. Wan, Y. Yang, C. Meneveau, R. Burns, S. Chen, A. Szalay, and G. Eyink, A public turbulence database cluster and applications to study Lagrangian evolution of velocity increments in turbulence, J. Turbul. **9**, N31 (2008).

[63] L. A. Martínez-Tossas, M. J. Churchfield, A. E. Yilmaz, H. Sarlak, P. L. Johnson, J. N. Sørensen, J. Meyers, and C. Meneveau, Comparison of four large-eddy simulation research codes and effects of model coefficient and inflow turbulence in actuator-line-based wind turbine modeling, J. Renewable Sustainable Energy **10**, 033301 (2018).

[64] LESGO: A parallel pseudo-spectral large-eddy simulation code, https://lesgo.me.jhu.edu.

[65] R. J. Stevens, J. Graham, and C. Meneveau, A concurrent precursor inflow method for Large Eddy Simulations and applications to finite length wind farms, Renewable Energy **68**, 46 (2014).

[66] R. J. Stevens and C. Meneveau, Temporal structure of aggregate power fluctuations in large-eddy simulations of extended wind-farms, J. Renewable Sustainable Energy **6**, 043102 (2014).

[67] S. A. Orszag and Y.-H. Pao, Numerical computation of turbulent shear flows, Adv. Geophys. **18A**, 225 (1975).

[68] J. H. Ferziger and M. Perić, *Computational Methods for Fluid Dynamics*, 1st ed. (Springer, Berlin, Germany, 1996).

[69] J. Albertson and M. Parlange, Surface length scales and shear stress: Implications for land-atmosphere interaction over complex terrain, Water Resour. Res. **35**, 2121 (1999).

[70] D. K. Lilly, The representation of small-scale turbulence in numerical simulation experiments, in

Proceedings of the IBM Scientific Computing Symposium on Environmental Sciences, edited by H. H. Goldstine (Yorktown Heights, New York, 1967), pp. 195–210.

[71] J. Smagorinsky, General circulation experiments with the primitive equations, Mon. Weather Rev. **91**, 99 (1963).

[72] E. Bou-Zeid, C. Meneveau, and M. Parlange, A scale-dependent Lagrangian dynamic model for large eddy simulation of complex turbulent flows, Phys. Fluids **17**, 025105 (2005).

[73] D. Yang, C. Meneveau, and L. Shen, Effect of downwind swells on offshore wind energy harvesting—A large-eddy simulation study, Renewable Energy **70**, 11 (2014).

[74] X. Yang and F. Sotiropoulos, LES investigation of infinite staggered wind-turbine arrays, J. Phys.: Conf. Ser. **555**, 012109 (2014).

[75] S. Xiao and D. Yang, Large-eddy simulation-based study of effect of swell-induced pitch motion on wake-flow statistics and power extraction of offshore wind turbines, Energies **12**, 1246 (2019).

[76] S. A. Orszag, Transform method for the calculation of vector-coupled sums: Application to the spectral form of the vorticity equation, J. Atmos. Sci. **27**, 890 (1970).

[77] J. D. Albertson, Large eddy simulation of land–atmosphere interaction, Ph.D. thesis, University of California, Davis, 1996.

[78] L. C. Pagnini, M. Burlando, and M. P. Repetto, Experimental power curve of small-size wind turbines in turbulent urban environment, Applied Energy **154**, 112 (2015).

[79] T. Stathopoulos, H. Alrawashdeh, A. Al-Quraan, B. Blocken, A. Dilimulati, M. Paraschivoiu, and P. Pilay, Urban wind energy: Some views on potential and challenges, J. Wind Eng. Ind. Aerodyn. **179**, 146 (2018).

[80] W. Xu, G. Li, X. Zheng, Y. Li, S. Li, C. Zhang, and F. Wang, High-resolution numerical simulation of the performance of vertical axis wind turbines in urban area: Part I, Wind turbines on the side of single building, Renewable Energy **177**, 461 (2021).

[81] W. Xu, Y. Li, G. Li, S. Li, C. Zhang, and F. Wang, High-resolution numerical simulation of the performance of vertical axis wind turbines in urban area: Part II, Array of vertical axis wind turbines between buildings, Renewable Energy **176**, 25 (2021).

[82] Y. Peng, Y. Xu, S. Zhan, and K. Shum, High-solidity straight-bladed vertical axis wind turbine: Aerodynamic force measurements, J. Wind Eng. Ind. Aerodyn. **184**, 34 (2019).

[83] V. Kumar, M. Paraschivoiu, and I. Paraschivoiu, Low reynolds number vertical axis wind turbine for Mars, Wind Eng. **34**, 461 (2010).

[84] N. Troldborg, J. N. Sorensen, and R. Mikkelsen, Numerical simulations of wake characteristics of a wind turbine in uniform inflow, Wind Energy **13**, 86 (2010).

[85] L. A. Martínez-Tossas, M. J. Churchfield, and C. Meneveau, Optimal smoothing length scale for actuator line models of wind turbine blades based on Gaussian body force distribution, Wind Energy **20**, 1083 (2017).

[86] T. von Kármán, *Aerodynamics* (McGraw-Hill, New York City, New York, 1963).

[87] M. M. Zdravkovich, *Flow around Circular Cylinders—Volume 1 : Fundamentals* (Oxford University Press, Oxford, England, UK, 1997).

[88] L. P. Chamorro, R. E. A. Arndt, and F. Sotiropoulos, Turbulent flow properties around a staggered wind farm, Boundary-Layer Meteorol. **141**, 349 (2011).

[89] Y.-T. Wu and F. Porté-Agel, Simulation of turbulent flow inside and above wind farms: Model validation and layout effects, Boundary-Layer Meteorol. **146**, 181 (2013).

[90] R. J. A. M. Stevens, D. F. Gayme, and C. Meneveau, Large eddy simulation studies of the effects of alignment and wind farm length, J. Renewable Sustainable Energy **6**, 023105 (2014).

[91] N. Jensen, A note on wind turbine interaction, Tech. Rep. No. Ris-M-2411 (RisøNational Laboratory, Roskilde, Denmark, 1983).

[92] M. Bastankhah and F. Porté-Agel, A new analytical model for wind-turbine wakes, Renewable Energy **70**, 116 (2014).

[93] C. Meneveau and J. Katz, Scale-invariance and turbulence models for large-eddy simulation, Annu. Rev. Fluid Mech. **32**, 1 (2000).

[94] S. P. Pope, *Turbulent Flows* (Cambridge University Press, Cambridge, England, UK, 2000).

[95] S. Pierre, *Large Eddy Simulation for Incompressible Flows: An Introduction* (Springer, Berlin, Germany, 2006).

[96] J. R. Baker, Features to aid or enable self starting of fixed pitch low solidity vertical axis wind turbines, J. Wind Eng. Ind. Aerodyn. **15**, 369 (1983).

[97] B. K. Kirke, Evaluation of self-starting vertical axis wind turbines for stand-alone applications, Ph.D. thesis, Griffith University, 1998.

[98] R. McGowan, R. Lozano, V. Raghav, and N. Komerath, Vertical axis micro wind turbine design for low tip speed ratios, in *Proceedings of the International Multi-Conference on Engineering and Technological Innovation* (2012), http://iiis.org/CDs2012/CD2012IMC/DEMSET_2012/PapersPdf/DC885ZU.pdf.

[99] M. Mahmoud, M. Ramadan, M. A. Abdelkareem, and A. G. Olabi, Introduction and definition of wind energy, in *Renewable Energy—Volume 1: Solar, Wind, and Hydropower*, edited by A. G. Olabi (Academic Press, Cambridge, MA, 2023), pp. 299–314.

[100] L. P. Chamorro, S.-J. Lee, D. Olsen, C. Milliren, J. Marr, R. E. A. Arndt, and F. Sotiropoulos, Turbulence effects on a full-scale 2.5 MW horizontal-axis wind turbine under neutrally stratified conditions, Wind Energy **18**, 339 (2015).

[101] S. Le Fouest and K. Mulleners, The dynamic stall dilemma for vertical-axis wind turbines, Renewable Energy **198**, 505 (2022).

[102] M. M. Miller, S. Duvvuri, and M. Hultmark, Solidity effects on the performance of vertical-axis wind turbines, Flow **1**, E9 (2021).

[103] W. J. McCroskey, The phenomenon of dynamic stall, Tech. Rep. No. 81264 (NASA, 1981).

[104] R. Gormont, A mathematical model of unsteady aerodynamics and radial flow for application to helicopter rotors, Tech. Rep. No. 72-67 (Army Air Mobility Research and Development Laboratory, 1973).

[105] P. Bachant and M. Wosnik, Characterising the near-wake of a cross-flow turbine, J. Turbul. **16**, 392 (2015).

[106] P. Schlatter, N. Adams, and L. Kleiser, A windowing method for periodic inflow/outflow boundary treatment of non-periodic flows, J. Comput. Phys. **206**, 505 (2005).

[107] S. Chester, C. Meneveau, and M. B. Parlange, Modeling turbulent flow over fractal trees with renormalized numerical simulation, J. Comput. Phys. **225**, 427 (2007).